ISSN 0253-9837
CN 21-1601/O6

催化学报 Chinese Journal of Catalysis

www.cjcatal.org

Volume 38 | Number 10 | October 2017

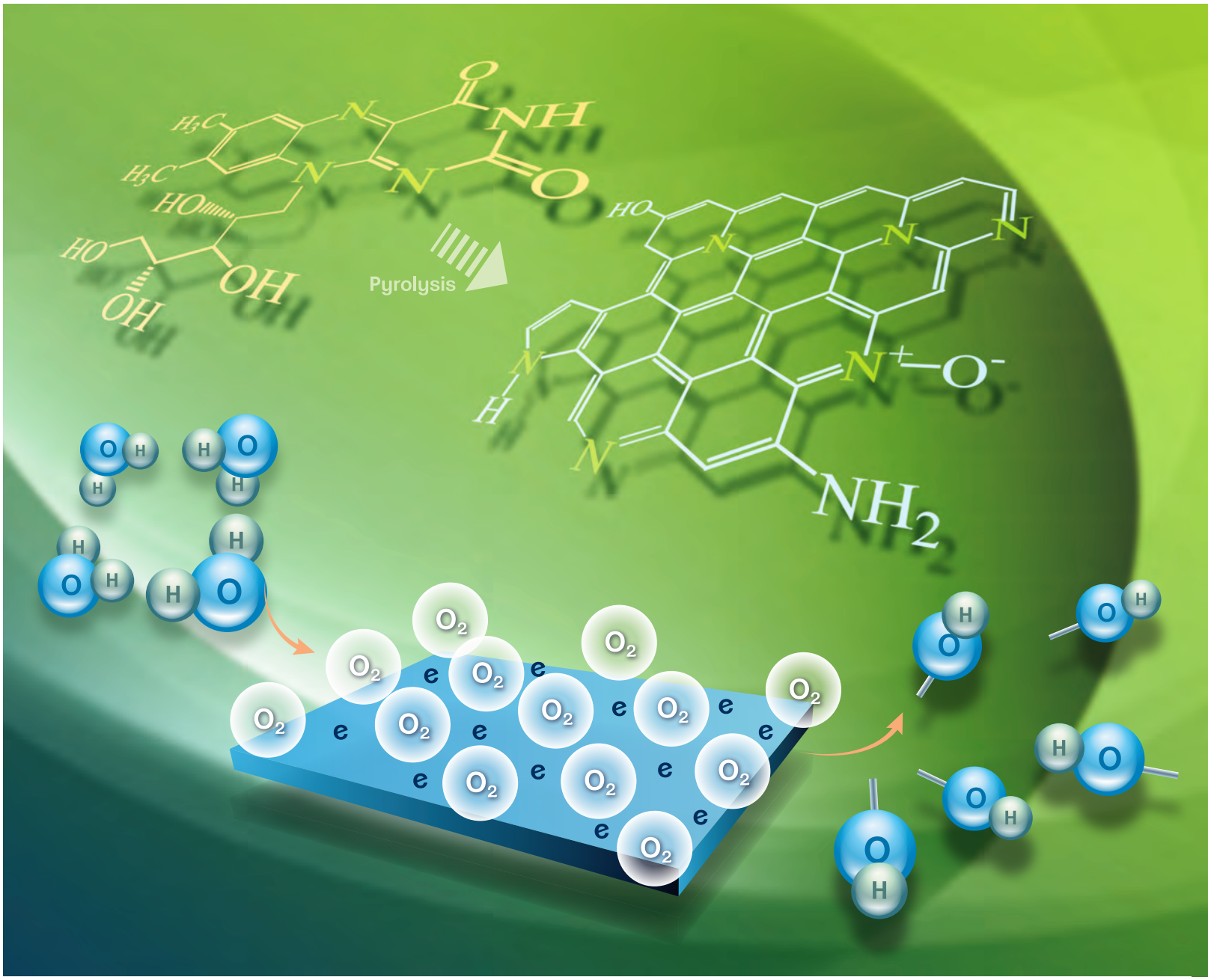

催化学报 CHINESE JOURNAL OF CATALYSIS October 2017 Vol. 38 No. 10 pages 1659–1779

科学出版社

Science Press

Editors-in-Chief Can Li (李灿) Tao Zhang (张涛)
Transaction of The Catalysis Society of China

2017
Vol. 38 No. 10

Chinese Journal of Catalysis

2017年
第38卷 第10期

In This Issue

Cover: Tang and coworkers in their Article on pages 1668–1679 reported a Fe–N–C catalyst via one–step pyrolysis in the presence of anhydrate iron chloride using cheap and nontoxic riboflavin as both carbon and nitrogen precursors. The picture shows the processes of catalyst preparation and oxygen reduction reaction, as well as the morphology of the catalyst.

封面: 唐水花等报道了以廉价无毒的核黄素作为碳氮源,一步热解制得 Fe–N–C 催化剂并将其应用于燃料电池阴极氧还原反应. 图片给出了催化剂制备和氧还原反应过程以及催化剂形貌. 见本期第 1668–1679 页.

About the Journal

Chinese Journal of Catalysis is an international journal published monthly by Chinese Chemical Society, Dalian Institute of Chemical Physics, Chinese Academy of Sciences, and Elsevier. The journal publishes original, rigorous, and scholarly contributions in the fields of heterogeneous and homogeneous catalysis in English or in both English and Chinese. The scope of the journal includes:

- New trends in catalysis for applications in energy production, environmental protection, and production of new materials, petroleum chemicals, and fine chemicals;
- Scientific foundation for the preparation and activation of catalysts of commercial interest or their representative models;
- Spectroscopic methods for structural characterization, especially methods for in situ characterization;
- New theoretical methods of potential practical interest and impact in the science and applications of catalysis and catalytic reaction;
- Relationship between homogeneous and heterogeneous catalysis;
- Theoretical studies on the structure and reactivity of catalysts.
- The journal also accepts contributions dealing with photo-catalysis, bio-catalysis, and surface science and chemical kinetics issues related to catalysis.

Types of Contributions

- ***Reviews*** deal with topics of current interest in the areas covered by this journal. Reviews are surveys, with entire, systematic, and important information, of recent progress in important topics of catalysis. Rather than an assemblage of detailed information or a complete literature survey, a critically selected treatment of the material is desired. Unsolved problems and possible developments should also be discussed. Authors should have published articles in the field. Reviews should have more than 80 references.
- ***Communications*** rapidly report studies with significant innovation and major academic value. They are limited to four Journal pages. After publication, their full-text papers can also be submitted to this or other journals.
- ***Articles*** are original full-text reports on innovative, systematic and completed research on catalysis.
- ***Highlights*** describe and comment on very important new results in the original research of a third person with a view to highlight their significance. The results should be presented clearly and concisely without the comprehensive details required for an original article.
- ***Perspectives*** are short reviews of recent developments in an established or developing topical field. The authors should offer a critical assessment of the trend of the field, rather than a summary of literatures.
- ***Viewpoints*** describe the results of original research in general in some area, with a view to highlighting the progress, analyzing the major problems, and commenting the possible research target and direction in the future.

Impact Factor

2016 SCI Impact Factor: **2.813**
2016 SCI 5-Year Impact Factor: 2.163
2015 ISTIC Impact Factor: 1.179

Abstracting and Indexing

Abstract Journals (VINITI)
Cambridge Scientific Abstracts (CIG)
Catalysts & Catalysed Reactions (RSC)
Current Contents/Engineering, Computing and Technology (Thomson ISI)
Chemical Abstract Service/SciFinder (CAS)
Chemistry Citation Index (Thomson ISI)
Japan Information Center of Science and Technology
Journal Citation Reports/Science Edition (Thomson ISI)
Science Citation Index Expanded (Thomson ISI)
SCOPUS (Elsevier)
Web of Science (Thomson ISI)

available at www.sciencedirect.com

ScienceDirect

journal homepage: www.elsevier.com/locate/chnjc

Chinese Journal of Catalysis

Graphical Contents

Perspective

Chin. J. Catal., 2017, 38: 1659–1663 doi: 10.1016/S1872-2067(17)62894-8

Titanocene dichloride: A new green reagent in organic chemistry

Antonio Rosales Martínez *, María Castro Rodríguez, Ignacio Rodríguez-García, Laura Pozo Morales, Roman Nicolay Rodríguez Maecker
University of Sevilla, Spain; University of Almería, Spain; Universidad de las Fuerzas Armadas-ESPE, Ecuador

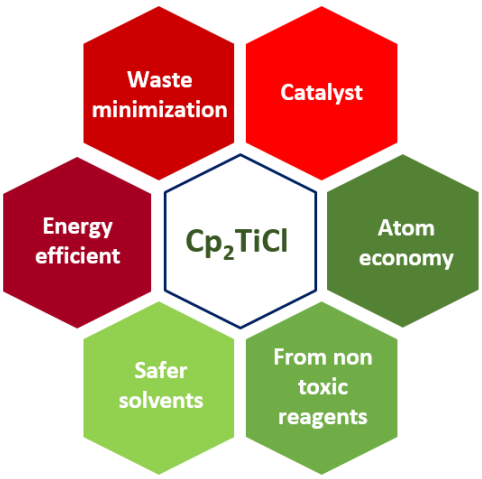

This review presents Cp_2TiCl as a new green reagent widely used in organic chemistry, with potential applications in fine chemistry, polymer chemistry and other fields.

Communication

Chin. J. Catal., 2017, 38: 1664–1667 doi: 10.1016/S1872-2067(17)62901-2

Direct construction of sulfenylated pyrazoles catalyzed by I_2 at room temperature

Shuang-Hong Hao, Li-Xia Li, Dao-Qing Dong, Zu-Li Wang *
Qingdao Agricultural University

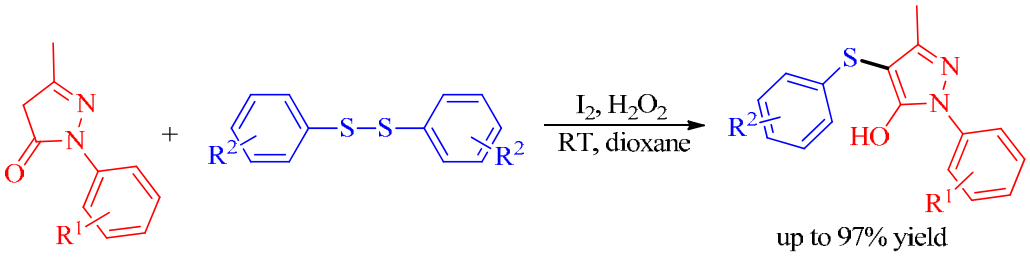

An iodine-catalyzed sulfenylation of pyrazoles at room temperature is described, in which a variety of pyrazoles were well tolerated and the desired products obtained in good to excellent yields.

Articles

Chin. J. Catal., 2017, 38: 1668–1679 doi: 10.1016/S1872-2067(17)62885-7

High performance ORR electrocatalysts prepared *via* one-step pyrolysis of riboflavin

Yuxiao Deng, Haixin Huangfu, Shuihua Tang *, Jie Li
Southwest Petroleum University

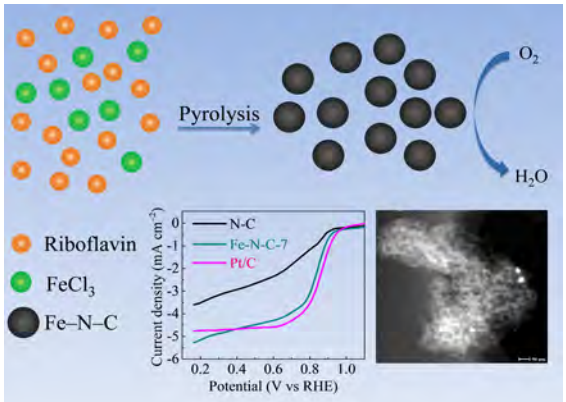

We report the synthesis of Fe–N–C catalysts *via* one-step pyrolysis using riboflavin as a cost-effective, nontoxic carbon and nitrogen precursor. A catalyst containing 7 wt% Fe demonstrates an excellent oxygen reduction reaction activity and stability.

Chin. J. Catal., 2017, 38: 1680–1687 doi: 10.1016/S1872-2067(17)62876-6

Catalytic performance and synthesis of a Pt/graphene-TiO_2 catalyst using an environmentally friendly microwave-assisted solvothermal method

Min Wang, Zhongwei Wang, Lu Wei, Jianwei Li, Xinsheng Zhao *
Jiangsu Normal University

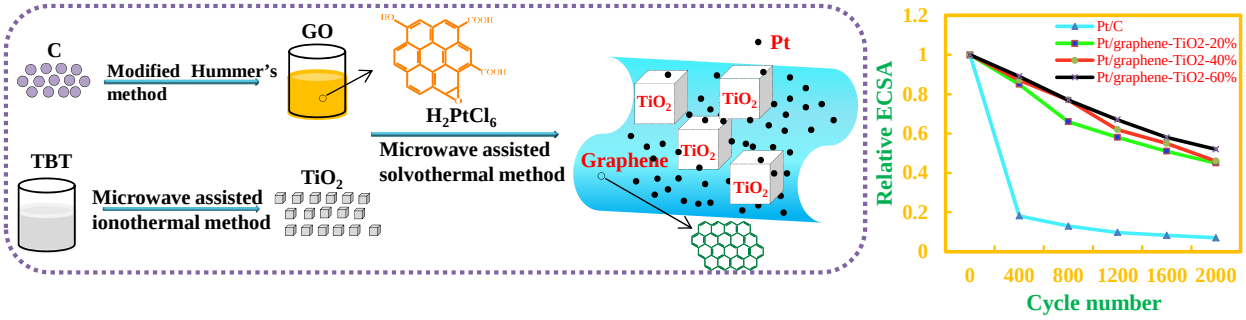

An environmentally friendly microwave-assisted method was developed for the synthesis of Pt/graphene-TiO_2 catalysts. The improved activity and stability of the nano-Pt catalysts were attributed to the high electronic conductivity and strong metal-support interactions.

Chin. J. Catal., 2017, 38: 1688–1696 doi: 10.1016/S1872-2067(17)62893-6

Influence of carbon and yttrium co-doping on the photocatalytic activity of mixed phase TiO_2

Honglin Gao, Jianmei Liu, Jin Zhang, Zhongqi Zhu, Genlin Zhang, Qingju Liu *
Yunnan University

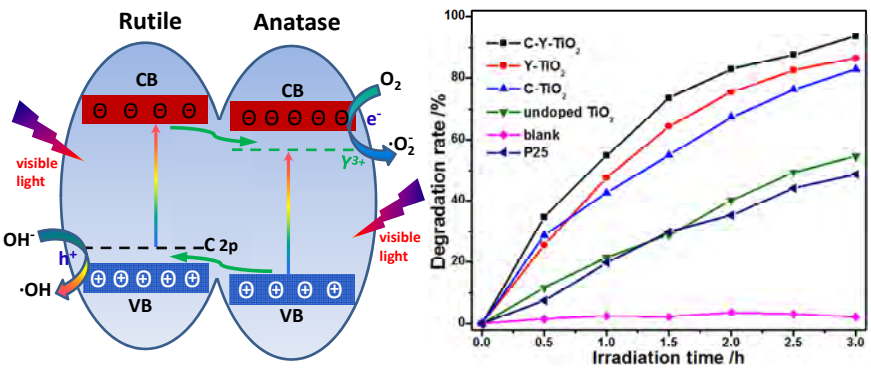

Carbon and Yttrium co-doping mixed phase TiO_2 has been fabricated by sol-gel method. The enhancement of photocatalytic activity can be attributed to the synergistic effect of C and Y co-doping and the appropriate crystalline structure.

Chin. J. Catal., 2017, 38: 1697–1710 doi: 10.1016/S1872-2067(17)62891-2

Coke-tolerant SiW_{20}-Al/Zr_{10} catalyst for glycerol dehydration to acrolein

Amin Talebian-Kiakalaieh, Nor Aishah Saidina Amin *
Universiti Teknologi Malaysia (UTM), Malaysia

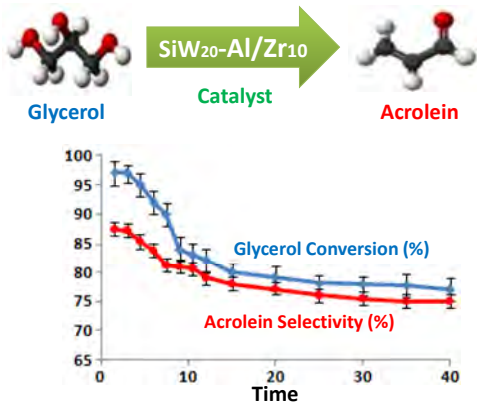

A coke-tolerant catalyst (SiW_{20}-Al/Zr_{10}), which gave 87.3% selectivity for acrolein and 97% glycerol conversion under the conditions 300 °C, 0.5 wt% catalyst, and 10 wt% feed concentration, was synthesized.

Chin. J. Catal., 2017, 38: 1711–1718 doi: 10.1016/S1872-2067(17)62907-3

One-step synthesis of graphitic carbon nitride nanosheets for efficient catalysis of phenol removal under visible light

Wang Ding, Suqin Liu *, Zhen He
Central South University

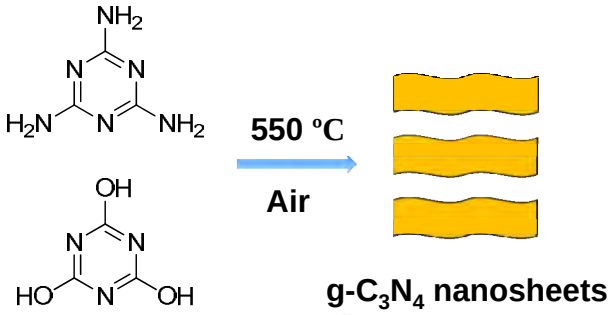

A simple method was developed to prepare g-C_3N_4 nanosheets by thermal polymerization of cyanuric acid and melamine in air. The g-C_3N_4 nanosheets showed superior photocatalytic activities than bulk g-C_3N_4.

Chin. J. Catal., 2017, 38: 1719–1725 doi: 10.1016/S1872-2067(17)62884-5

Novel-structured Mo-Cu-Fe-O composite for catalytic air oxidation of dye-containing wastewater under ambient temperature and pressure

Yin Xu *, Henan Shao, Fei Ge, Yun Liu
Xiangtan University

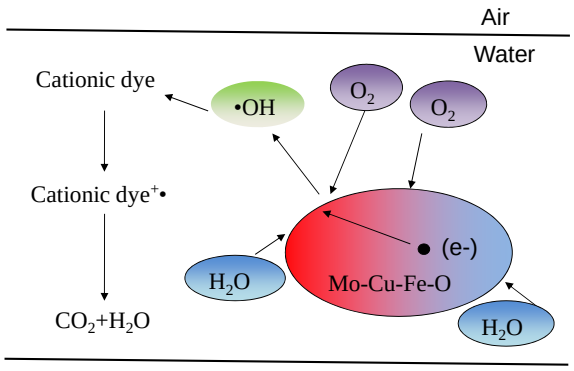

A novel-structured Mo-Cu-Fe-O composite showed superior catalytic activity for the degradation of cationic dyes in wastewater through the generation of hydroxyl radicals.

Chin. J. Catal., 2017, 38: 1726–1735 doi: 10.1016/S1872-2067(17)62902-4

Synthesis of Ag/AgCl/Fe-S plasmonic catalyst for bisphenol A degradation in heterogeneous photo-Fenton system under visible light irradiation

Yun Liu *, Yanyan Mao, Xiaoxiao Tang, Yin Xu, Chengcheng Li, Feng Li
Xiangtan University

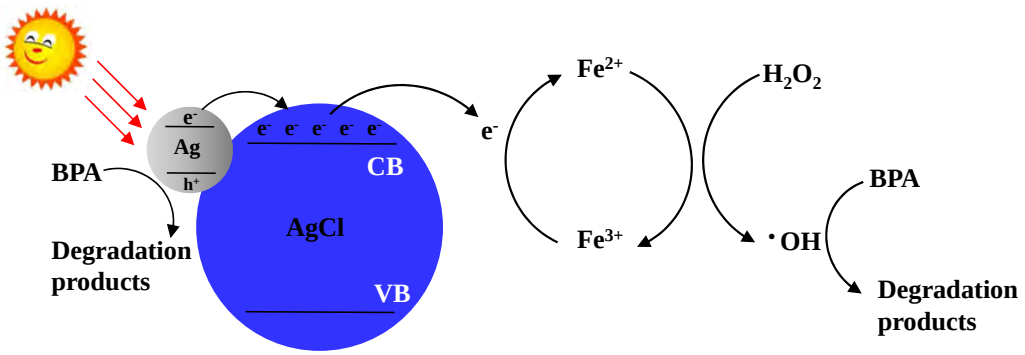

In a heterogeneous photo-Fenton system ·OH radicals and holes are the major active species contributing to the high photocatalytic activity of Ag/AgCl/Fe-S catalyst.

Chin. J. Catal., 2017, 38: 1736–1748 doi: 10.1016/S1872-2067(17)62883-3

Influence of nickel(II) oxide surface magnetism on molecule adsorption: A first-principles study

Chuan-Qi Huang, Wei-Xue Li *
Dalian Institute of Chemical Physics, Chinese Academic of Sciences;
University of Chinese Academy of Sciences;
University of Science and Technology of China

Calculations revealed that NO preferentially binds to Ni surfaces with its magnetic moment antiparallel to that of Ni. NO adsorbed at anti-ferromagnetic bridge sites binds to one Ni optimally and another in a frustrated manner.

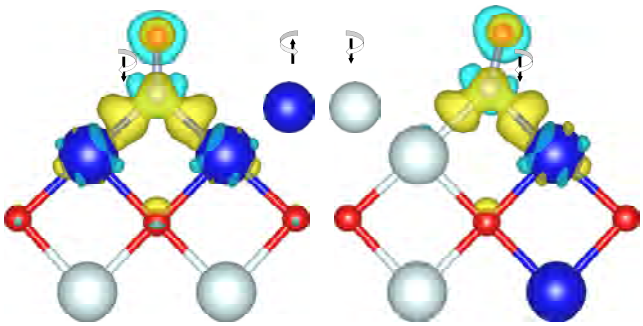

Chin. J. Catal., 2017, 38: 1749–1758 doi: 10.1016/S1872-2067(17)62887-0

Catalytic performance of highly dispersed WO_3 loaded on CeO_2 in the selective catalytic reduction of NO by NH_3

Lei Zhang, Jingfang Sun, Yan Xiong, Xiaoqing Zeng, Changjin Tang, Lin Dong *
Chongqing Three Gorges University; Nanjing University; Nanyang Normal University

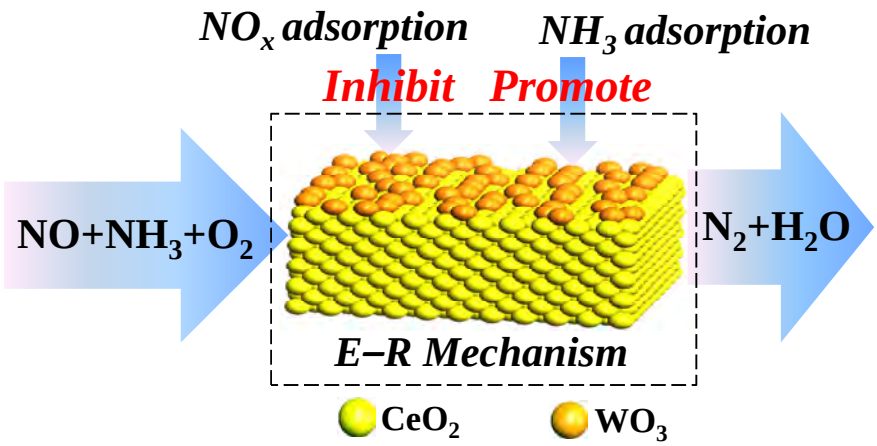

WO_3 dispersed on the CeO_2 surface inhibits adsorption of NO_x species and promotes NH_3 adsorption on supported WO_3/CeO_2 catalysts, which promotes the NH_3 selective catalytic reduction reaction via the Eley-Rideal (E-R) route.

Chin. J. Catal., 2017, 38: 1759–1769 doi: 10.1016/S1872-2067(17)62890-0

A novel process of ozone catalytic oxidation for low concentration formaldehyde removal

Bin Zhu, Xiao-Song Li, Peng Sun, Jing-Lin Liu, Xiao-Yuan Ma, Xiaobing Zhu *, Ai-Min Zhu *
Dalian Maritime University; Dalian University of Technology

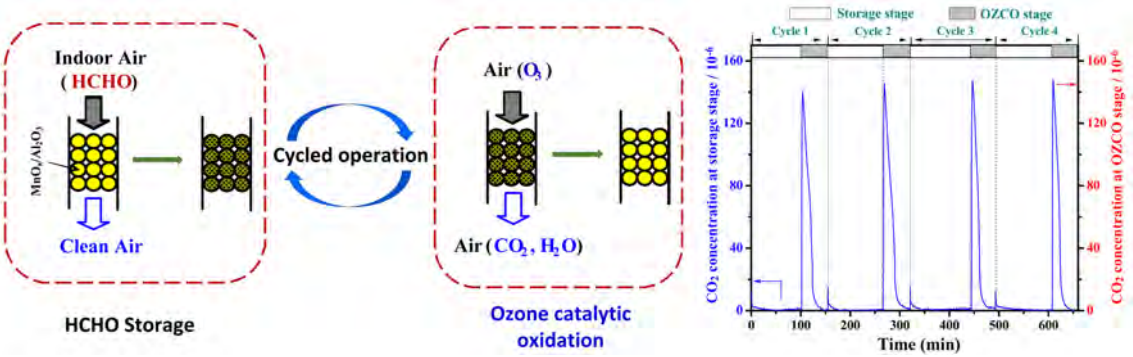

A promising novel process of cycled storage-ozone catalytic oxidation (OZCO) was successfully employed to remove low concentration formaldehyde (HCHO) from air over the optimal MnO_x/Al_2O_3 catalyst (manganese acetate precursor and 10 wt% Mn loading) at room temperature.

Chin. J. Catal., 2017, 38: 1770–1779 doi: 10.1016/S1872-2067(17)62888-2

Visible light-responsive carbon-decorated p-type semiconductor $CaFe_2O_4$ nanorod photocatalyst for efficient remediation of organic pollutants

Xin Liu, Yuhong Zhang, Yushuai Jia *, Junzhe Jiang, Yabin Wang, Xiangshu Chen *, Tian Gui
Jiangxi Normal University

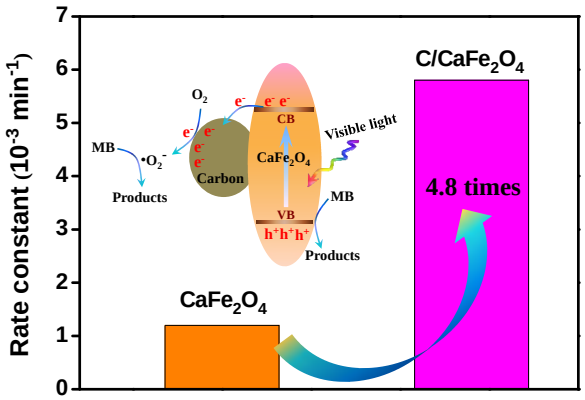

Carbon-decorated p-type semiconductor $CaFe_2O_4$ nanorods exhibit an enhanced photocatalytic activity for the degradation of MB owing to the simultaneous improvement of MB adsorption, separation and transfer of photogenerated charges and light absorption.

中国科学院科学出版基金资助出版

Chinese Journal of Catalysis 催化学报

月刊 SCI收录 2017年10月 第38卷 第10期

目 次

视 角

1659
Cp_2TiCl: 有机化学中广泛使用的新绿色试剂
Antonio Rosales Martínez , María Castro Rodríguez, Ignacio Rodríguez-García, Laura Pozo Morales, Roman Nicolay Rodríguez Maecker

快 讯

1664
室温下碘催化直接构建硫化吡唑啉酮
郝双红，李丽霞，董道青，王祖利

论 文

1668
一步热解核黄素制备高性能氧还原反应电催化剂
邓玉潇，皇甫海新，唐水花，李杰

1680
微波辅助溶剂热法制备Pt/石墨烯-TiO_2及其催化性能
王敏，王中伟，韦露，李建伟，赵新生

1688
碳和钇共掺杂对混相TiO_2光催化性能的影响
高洪林，刘健梅，张瑾，朱忠其，张艮林，柳清菊

1697
容碳的SiW_{20}-Al/Zr_{10}催化剂用于甘油脱水制丙烯醛
Amin Talebian-Kiakalaieh, Nor Aishah Saidina Amin

1711
一步法合成g-C_3N_4纳米片用作苯酚可见光降解高效催化剂
丁望，刘素琴，何震

1719
常温常压湿式催化氧化染料废水的Mo-Cu-Fe-O新型复合催化材料
许银，邵贺楠，葛飞，刘云

1726
Ag/AgCl/铁-海泡石异相可见光Fenton催化降解双酚A
刘云，毛妍彦，唐宵宵，许银，李程程，李峰

1736
NiO表面磁性对分子吸附的影响的第一性原理研究
黄传奇，李微雪

1749
CeO_2表面分散态WO_3的氨选择性催化还原性能
张雷，孙敬方，熊燕，曾小清，汤常金，董林

1759
臭氧催化氧化脱除低浓度甲醛的新方法
朱斌，李小松，孙鹏，刘景林，马晓媛，朱晓兵，朱爱民

1770
可见光响应的碳修饰纳米棒状p型$CaFe_2O_4$半导体光催化降解有机污染物
刘鑫，张玉红，贾玉帅，姜君哲，王亚斌，陈祥树，桂田

英文全文电子版(国际版)由Elsevier出版社在ScienceDirect上出版
http://www.sciencedirect.com/science/journal/18722067
http://www.elsevier.com/locate/chnjc
www.cjcatal.org
在线投审稿网址
https://mc03.manuscriptcentral.com/cjcatal

Chinese Journal of Catalysis 38 (2017) 1736–1748 催化学报 2017年 第38卷 第10期 | www.cjcatal.org

available at www.sciencedirect.com

ScienceDirect

journal homepage: www.elsevier.com/locate/chnjc

Article

Influence of nickel(II) oxide surface magnetism on molecule adsorption: A first-principles study

Chuan-Qi Huang [a,b], Wei-Xue Li [a,b,c,*]

[a] State Key Laboratory of Catalysis, Dalian Institute of Chemical Physics, Chinese Academic of Sciences, Dalian 116023, Liaoning, China

[b] University of Chinese Academy of Sciences, Beijing 100049, China

[c] Department of Chemical Physics, College of Chemistry and Materials Science, iChEM, CAS Center for Excellence in Nanoscience, Hefei National Laboratory for Physical Sciences at the Microscale, University of Science and Technology of China, Hefei 230026, Anhui, China

ARTICLE INFO

Article history:
Received 27 May 2017
Accepted 26 June 2017
Published 5 October 2017

Keywords:
Magnetism
Surface orientation
Molecule adsorption
First-principles theory
Electronic structure

ABSTRACT

The influence of the magnetism of transition metal oxide, nickel(II) oxide (NiO), on its surface reactivity and the dependence of surface reactivity on surface orientation and reactant magnetism were studied by density functional theory plus U calculations. We considered five different antiferromagnetically ordered structures and one ferromagnetically ordered structure, NiO(001) and Ni(011) surfaces, paramagnetic molecule NO, and nonparamagnetic molecule CO. The calculations showed that the dependence of surface energies on magnetism was modest, ranging from 49 to 54 meV/Å^2 for NiO(001) and from 162 to 172 meV/Å^2 for NiO(011). On NiO(001), both molecules preferred the top site of the Ni cation exclusively for all NiO magnetic structures considered, and calculated adsorption energies ranged from −0.33 to −0.37 eV for CO and from −0.42 to −0.46 eV for NO. On NiO(011), both molecules preferred the bridge site of two Ni cations irrespective of the NiO magnetism. It was found that rather than the long-range magnetism of bulk NiO, the local magnetic order of two coordinated Ni cations binding to the adsorbed molecule had a pronounced influence on adsorption. The calculated NO adsorption energy at the (↑↓) bridge sites ranged from −0.99 to −1.05 eV, and become stronger at the (↑↑) bridge sites with values of −1.21 to −1.30 eV. For CO, although the calculated adsorption energies at the (↑↓) bridge sites (−0.73 to −0.75 eV) were very close to those at the (↑↑) bridge sites (−0.71 to −0.72 eV), their electron hybridizations were very different. The present work highlights the importance of the local magnetic order of transition metal oxides on molecular adsorption at multi-fold sites.

© 2017, Dalian Institute of Chemical Physics, Chinese Academy of Sciences.
Published by Elsevier B.V. All rights reserved.

1. Introduction

Transition metal oxide (TMO) surfaces currently have a wide range of applications in energy and environmental science, such as catalysts for clean energy conversion, cleanup of air pollutants, and sensors for chemical and biomedical devices [1,2]. Understanding the surface chemistry and structure–activity relationship of TMOs is therefore important for the further development of these applications [3]. In particular, 3*d* TMOs are notable because of their involved spin states and magnetism, which is sensitive to surface orientation and particle size [4–7]. For instance, the spin states of Co ions (rather than number of 3*d* electrons) in perovskite oxides play a critical role in their oxygen evolution activity [8]. In addition to

* Corresponding author. Tel: +86-551-63600650; E-mail: wxli70@ustc.edu.cn
This work was supported by the National Natural Science Foundation of China (91645202), the National Key R&D Program of China (2017YFB602205), the National Basic Research Program of China (2013CB834603), and the Frontier Science Key Project of Chinese Academy of Sciences (QYZDJ-SSW-SLH054).
DOI: 10.1016/S1872-2067(17)62883-3 | http://www.sciencedirect.com/science/journal/18722067 | Chin. J. Catal., Vol. 38, No. 10, October 2017

oxides, the spin states of molecules such as O_2 influence their corresponding dissociation activity on oxides [9] and even simple metal surfaces [10]. Magnetism can be induced in metal oxides that are paramagnetic in bulk by surface adsorption and reaction [11,12]. It is therefore interesting to study the influence of the spin states and magnetism of oxides on their surface chemistry.

Late 3*d* transition metal monoxides (MnO, FeO, CoO, and NiO) with cubic rock salt structure ($Fm\bar{3}m$) [13,14] are of particular importance in the study of antiferromagnetic (AFM) TMOs, and are often considered as model AFM systems. Besides their relatively high Neel temperature (T_N) and chemical stability, their large band gap (E_G) and insulating electronic structure allow their magnetic properties to be accurately described in terms of magnetic moments localized on transition metal cations [15,16]. The anisotropic interaction between neighboring magnetic moments leads to long-range magnetic ordering, known as type-2 antiferromagnetism (AFM2), below T_N [17–20] and stacking of ferromagnetic (FM) (111) planes with opposite spin directions in adjacent layers, as identified by neutron diffraction [21]. Using magnetic exchange force microscopy, the magnetic order of surface nickel ions on the NiO(001) surface has been measured directly in real space [22–26]. Despite the definite AFM order of magnetic ions in the perfect bulk crystal below T_N, the ordering of magnetic ions on the surface can be changed under different conditions. For example, by engineering defects in the lattice of AFM NiO, a FM ordering dislocation can be introduced [27]. When the size of AFM NiO decreases to the nanoscale, the resulting decrease of coordination and lattice distortion can drive the phase transition to a FM-like phase [27,28].

The magnetism of metal ions in late 3*d* TMOs originates from their partially filled 3*d* states, which are famous for their highly correlated nature [29]. It remains challenging to accurately describe strongly localized and correlated *d* electrons using standard density functional theory (DFT) approaches such as the local density approximation (LDA) or generalized gradient approximation (GGA) [30,31]. Both the LDA and GGA often fail to predict E_G of these TMOs [32]. For instance, both CoO and FeO were predicted to be metallic. Although NiO and MnO were predicted to have E_G, the calculated values were severely underestimated [33]. Nevertheless, E_G of these materials can be opened in calculations by adding a Hubbard U term describing the strong on-site Coulomb repulsion to the LDA or GGA (DFT+U) [34,35]. Compared to higher-level theories such as the hybrid functional or many-body perturbation [31,36], DFT+U can substantially improve the calculation accuracy without increasing the computational cost, as demonstrated for the adsorption of CO and NO on NiO(001) [37,38]. Simulation of water dissociative adsorption on NiO(111) was reported recently, and the calculation was found to be fairly insensitive to the choice of the DFT+U functional [39].

Chemically equivalent oxide surfaces may become inequivalent when considering the different symmetry of various long-range magnetisms. Because surface chemistry is largely decided by local environment (geometry and composition), it is currently unclear how the different magnetisms affect surface chemistry. Furthermore, the influence of different surfaces on magnetisms is still unknown. This influence may be mediated by reactants with different spin and/or magnetic moments. To clarify these issues, here NiO as a model system is studied by the GGA +U method. A number of magnetic phases, including AFM1, AFM2, AFM3, AFM4, AFM5, and FM, are considered. NiO(001) and NiO(110) surfaces are used to study the sensitivity of these magnetic phases to structure. While CO and NO adsorbed on NiO(001) of AFM2 has been studied to verify the DFT+U scheme treatment for strongly correlated systems [37,38], here we use the adsorption of paramagnetic molecule NO and nonparamagnetic molecule CO to probe the influence of magnetism on molecule adsorption by NiO surfaces.

2. Computational details

DFT calculations were performed with the Vienna ab initio simulation package (VASP) [40] based on the projected augmented wave (PAW) method [41,42]. The spin-polarized Perdew Burke Ernzerhof (PBE) [43] exchange-correlation functional and on-site Coulomb repulsion U term for *d* electrons in the spirit of Hubbard according to Dudarev's approach [35] were used to describe electron exchange and correlation. An effective U of 5.3 eV for Ni was used throughout the present work, because it could reproduce well bulk properties and CO/NO adsorption on NiO(001) surfaces [37].

Because partially occupied *d* orbitals are strongly localized at Ni^{2+}, a net spin magnetic moment was assigned to each Ni^{2+}. For the cubic sublattice of magnetic ions, all magnetic ions having parallel spin means there is FM order (Figure 1(a)). In

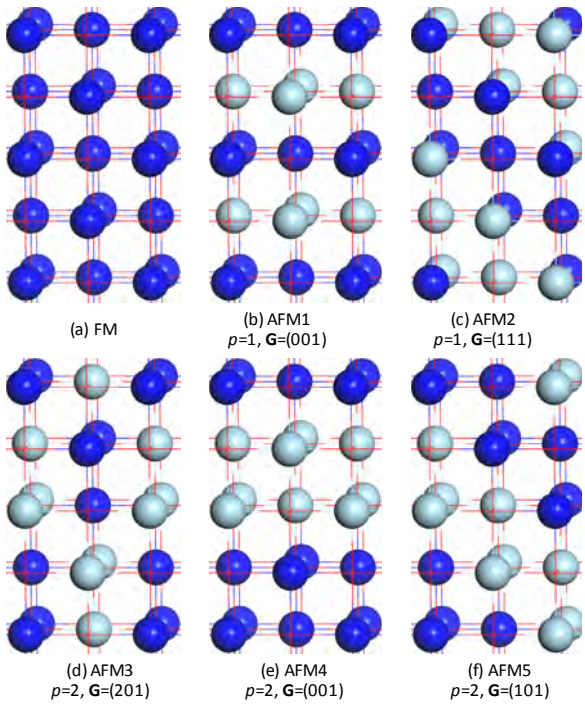

Fig. 1. Schematic illustration of NiO ferromagnetism FM (a), antiferromagnetism AFM1 (b), AFM2 (c), AFM3 (d), AFM4 (e) and AFM5 (f). Line cross points represent O, blue balls represent Ni spin up, and white balls represent Ni spin down.

contrast, the series of common AFM configurations of Ni^{2+} AFM1–AFM5 (as shown in Figure 1(b–f)) can be described as oppositely stacked FM layers in direction G with super lattice periodicity p in which Ni^{2+} maintain parallel spin within p layers [44]. Below T_N = 523 K, the ground-state magnetic configuration of NiO is AFM2 [21]. We considered AFM1–AFM5 and FM magnetic order as a starting point to construct surfaces with different surface magnetic order by truncation of bulk NiO.

Four layers of an NiO(001) slab ($2\sqrt{2}\times2\sqrt{2}$) surface supercell and five layers of an NiO(011) slab (4×4) surface supercell were used to model the adsorption of molecules on NiO(001) and NiO(011) surfaces, respectively. Slabs were separated by 12 Å of vacuum with the bottom two layers fixed at the bulk truncated structure, and dipole correction perpendicular to each slab was imposed. The layer thickness and vacuum size were found to converge for adsorption of CO/NO on AFM2. Surface energy was evaluated with symmetric slabs of the minimum surface cell for each surface until they converged to less than 1 meV/Å^2 with respect to slab thickness. A plane wave cutoff of 400 eV and k-point grids of (4×4×1) for NiO(001)-($2\sqrt{2}\times2\sqrt{2}$) and (3×2×1) for NiO(011)-(2×4) were used. Geometrical optimization was performed until the force on relaxed atoms was less than 0.02 eV/Å.

3. Results and discussion

3.1. NiO bulk

Table 1 lists the optimized equilibrium lattice constant, energy difference per NiO formula with respect to the lowest energy state (AFM2), localized magnetic moment on Ni, and band gap for the various magnetic phases considered. The energetically most favorable long-range magnetic phase is AFM2, which is consistent with the structure of NiO below T_N determined by neutron diffraction. The energy difference between different magnetic phases can be as large as 102 meV/NiO. AFM2 has the smallest lattice constant (a = 4.19 Å) and magnetic moment of Ni (m =1.71 μ_B), but the largest E_G of 3.25 eV for the magnetic phases. The present work agrees well with the results of a previous SGGA+U calculation (a = 4.20 Å, m = 1.72 μ_B, E_G = 3.2 eV) [37]. For the other AFM phases, the lattice constant and magnetic moment increase by 0.02 Å and 0.10 μ_B at most, respectively, but E_G decreases by 1.16 eV. It is clear that the lower the energy of the magnetic phase, the smaller the lattice constant and magnetic moment and the larger the E_G. These trends originate from the superexchange interaction of the second nearest neighbor (NN) Ni^{2+}, as rationalized in an earlier theory for rock salt transition metal monoxides [33,45].

Table 1
Energy difference per NiO formula with respect to the lowest state (AFM2) (ΔE), equilibrium lattice constant (a), localized magnetic moment on Ni (M), and energy band gap (E_G) of various magnetism phases.

	ΔE/meV	a/Å	M/μ_B	E_G/eV
AFM1	101	4.21	1.81	2.20
AFM2	0	4.19	1.71	3.25
AFM3	65	4.20	1.77	2.51
AFM4	61	4.20	1.77	2.26
AFM5	30	4.19	1.74	2.88
FM	91	4.21	1.80	2.09

To understand the origin of the AFM behavior of NiO, we fitted the calculated energy in Table 1 to the Ising model of magnetic moment interaction [19]. The fitting result gives i-th NN magnetic moment exchange pair interactions J_i (i = 1, 2, 3, and 4) of 0.71, −15.58, −0.24, and 0.07 meV, respectively. This means that the second NN interaction (J_2) is the dominant interaction and the negative value indicates the preference for AFM order, similar to the behavior of CoO and MnO [18,19]. Because J_1, J_3, and J_4 are much smaller than J_2, the number of second NN pairs determines the relative stability of the various AFM phases. For AFM2, all the second NN pairs are antiparallel, so it is energetically the most favorable state of NiO.

In this work, a Ni atom with an upward (or positive) magnetic moment (↑) means that the electron population of the spin-up component is larger than that of the spin-down, whereas a Ni atom with a downward (or negative) magnetic moment (↓) means that the electron population of the spin-down component is larger than that of the spin-up. The spin-resolved density of states (SDOS) of Ni (↑) in bulk NiO-AFM2 is illustrated in Figure 2. For the $3d_{xy,yz,xz}$ (t_{2g}) band, both the spin-up and spin-down components are distributed in the valence band. Compared with the spin-up component, the electrons in the spin-down component mainly populate the upper/top part of the valence band. For the $3d_{x^2-y^2,z^2}$ (e_g) band, the marked exchange splitting causes the e_g states to be well separated (by ~9.69 eV). In particular, the spin-down components are distributed in the conduction band. Most of the spin-up components are distributed in the lower part of the valence band, and a small amount are distributed close to the top of the valence band. The gap between the valence band maximum (VBM) and conduction band minimum (CBM) of the Ni 3d band is 3.23 eV, which is nearly same with as the E_G of bulk NiO (3.25 eV). For Ni(↓), the corresponding components are simply reversed. As shown below, these features are essential for the hybridization between Ni and CO/NO molecules.

3.2. NiO(001)

3.2.1. Surface properties

For rock salt crystals, the (001) plane is chemically equivalent with (010), (100), (00$\bar{1}$), (0$\bar{1}$0), and ($\bar{1}$00): all belong to the {001} plane family, and the corresponding primitive cell is (1×1). A long-range magnetic phase lowers the corresponding symmetry and decreases the degeneracy of the {001} plane family. The nonequivalent planes depended on the long-range magnetic phase (AFM1–AFM5), as classified in Table 2 and plotted in Figure 3. Each of AFM1, AFM3, AFM4, and AFM5 had two nonequivalent planes, whereas AFM2 had only one nonequivalent plane. This led to nine nonequivalent surfaces with different primitive cells, although they are all chemically equivalent.

Taking AFM1-(100) (Figure 3(b)) as an example, the magnetic moments of the first NN Ni pair are exclusively antiparal-

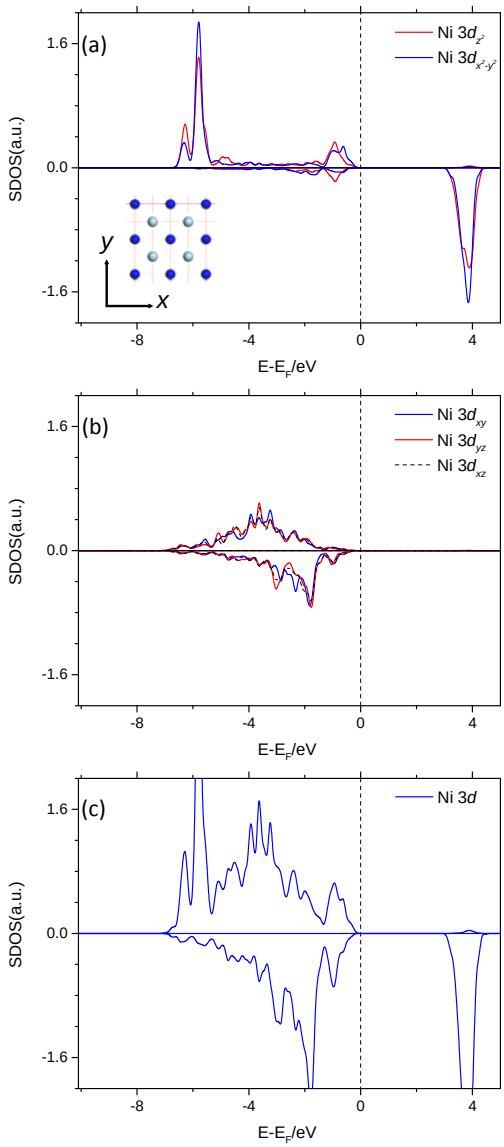

Fig. 2. Spin-resolved projected density of states (SDOS) for Ni in bulk AFM2 NiO. (a) SDOS projected onto Ni $3d_{z^2}$, $3d_{x^2-y^2}$; (b) SDOS projected onto Ni $3d_{xy}$, $3d_{yz}$, $3d_{xz}$; (c) Total SDOS of Ni 3*d*. The reference coordinates for DOS projection is shown in inset of (a), where *x*-axis represents for [100] direction and *y*-axis for [010] direction.

lel (↑↓). Similar behavior was found for AFM3-(001) (Figure 3(d)). In contrast, for AFM1-(001) (Figure 3(a)) and AFM4-(001) (Figure 3(f)), the magnetic moments of the first NN Ni pair are exclusively parallel (↑↑). For the remaining five surfaces shown in Figure 3, both the (↑↓) and (↑↑) configurations coexist in the first NN Ni pairs, forming different surface magnetism patterns. The different local magnetic pairs along with their long-range magnetic phases provide a good playground to investigate the influence of magnetism on surface properties. Figure 4 plots the SDOS of a surface Ni atom (↑) from AFM2-(001). The overall features remain the same as that of AFM2 bulk (Figure 2). The main difference is the gap between the VBM and CBM of the Ni 3*d* band, which decreases from the bulk value of 3.23 to 2.81 eV.

The calculated surface energies are presented in Table 2.

Table 2
Nonequivalent surfaces of rock salt NiO{001} family taking into account of magnetism, though in each column the surfaces remain equivalent. Corresponding surface energy γ (meV/Å²) is given, and as reference for FM(001), γ = 50 meV/Å².

	AFM1		AFM2	AFM3		AFM4		AFM5	
γ	49	50	54	54	51	54	52	52	54
	(001)	(100)	(001)	(001)	(010)	(001)	(010)	(001)	(010)
	(00$\bar{1}$)	($\bar{1}$00)	(00$\bar{1}$)	(00$\bar{1}$)	(0$\bar{1}$0)	(00$\bar{1}$)	(0$\bar{1}$0)	(00$\bar{1}$)	(0$\bar{1}$0)
		(010)	(010)		(100)		(100)	(100)	
		(0$\bar{1}$0)	(0$\bar{1}$0)		($\bar{1}$00)		($\bar{1}$00)	($\bar{1}$00)	
			(100)						
			($\bar{1}$00)						

The surface energies range from 49 to 54 meV/Å², and the difference between different magnetic phases is less than 5 meV/Å². To rationalize this small variation, we note that the surface energy increases mainly from the cost of Ni–O bond cleavage when creating a new surface. Considering the exchange coupling between magnetic cations, cleavage of the Ni–O bond might introduce an additional cost originating from the loss of the corresponding exchange interaction. Because the exchange interaction between Ni^{2+} is largely determined by J_2, the estimated cost of breaking the J_2 interaction when creating a new surface is ~1.7 meV/Å². Namely, the contribution from the long-range AFM phases to the surface energy is indeed small. Compared to the calculated overall surface energy, the contribution from magnetism (~3%) is negligible.

3.2.2. *Adsorption of CO and NO molecules*

CO and NO adsorption on these nonequivalent surfaces at a coverage of 0.25 monolayer with respect to surface Ni was

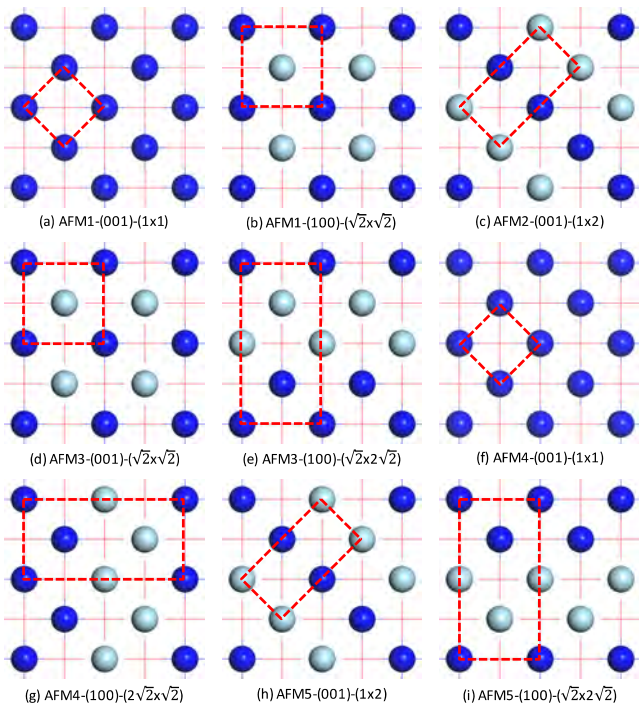

Fig. 3. Top view configuration of various nonequivalent NiO(001) surfaces taking into account of magnetism. Surface primitive cells are marked by frame of red dash line.

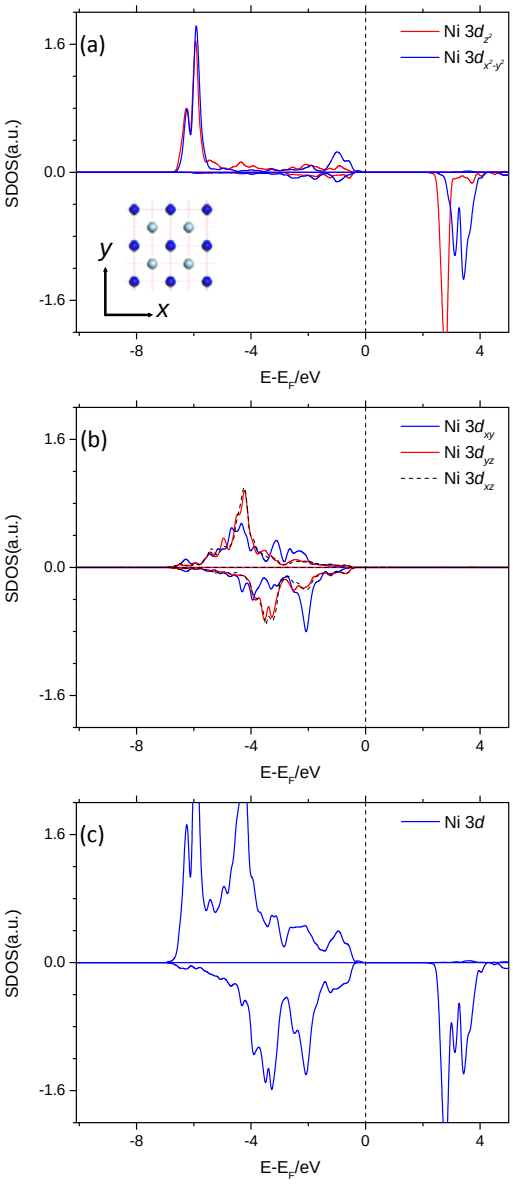

Fig. 4. Spin-resolved projected density of states (SDOS) for upward magnetic moment Ni(↑) of clean NiO AFM2(001). (a) SDOS projected onto Ni $3d_{z^2}$, $3d_{x^2-y^2}$; (b) SDOS projected onto Ni $3d_{xy}$, $3d_{yz}$, $3d_{xz}$; (c) Total SDOS of Ni 3*d*. The reference coordinates for DOS projection is shown in inset of (a), where *x*-axis represents for [100] direction and *y*-axis for [010] direction.

studied. Various adsorption sites were considered, and the results for adsorption at the energetically most favorable sites are given in Table 3. For the nonequivalent surfaces considered, calculated CO adsorption energies varied from −0.33 to −0.37 eV, while NO adsorption energies were more exothermic and ranged from −0.42 to −0.46 eV. The small change of adsorption energies (0.04 eV; less than 10%) reveals the weak influence of the long-range magnetic phases on both CO and NO adsorption. The calculated adsorption energies are in good agreement with those obtained from a previous GGA+U calculation on a (001) surface of NiO with AFM2 magnetic order and thermodesorption and infrared experiments (−0.30 to −0.45 eV for CO and −0.52 to −0.57 eV for NO) [37,38,46–48].

Table 3
Magnetism and structure information of CO adsorption on NiO {001}. Magnetic moment (M_{Ni}, M_{CO}) is given in unit of μ_B. Adsorption energy of CO E_{ads} is given in eV. Bond length ($d_{Ni\text{-}C}$) is given in Å.

	$M_{Ni(clean)}(\uparrow)/\mu_B$	$M_{Ni}(\uparrow)/\mu_B$	M_{CO}/μ_B	$d_{Ni\text{-}C}$/Å	E_{ads}/eV
AFM1(001)	1.80	1.78	0.01	2.04	−0.34
AFM1(100)	1.81	1.78	0.02	2.05	−0.34
AFM2(001)	1.72	1.69	0.01	2.07	−0.36
AFM3(001)	1.78	1.76	0.02	2.05	−0.33
AFM3(100)	1.77	1.74	0.01	2.04	−0.34
AFM4(001)	1.78	1.76	0.01	2.05	−0.34
AFM4(100)	1.77	1.74	0.02	2.04	−0.35
AFM5(001)	1.74	1.70	0.01	2.02	−0.37
AFM5(100)	1.75	1.72	0.02	2.04	−0.34
FM(001)	1.80	1.77	0.02	2.05	−0.35

In line with its weak binding strength, CO adsorption induces little change of the magnetism (less than 0.02 μ_B) of CO and coordinated Ni atom. As shown in Figure 5(a), CO adsorbed nearly perpendicularly at the top of a Ni atom. The optimized Ni–C bond length varied from 2.02 to 2.07 Å, where a shorter bond length indicates stronger binding. Meanwhile, the C–O bond length of 1.14 Å was the same as that of gas-phase CO. Small tilting of the angle between the Ni–C and C–O bonds could be energetically favorable; however, the variation of the corresponding potential energy surface was less than 10 meV for tilt angles up to 30° [37].

The bonding mechanism between CO and a coordinated Ni atom can be inferred from the corresponding SDOS plotted in Figure 5(b). The hybridization is mainly between the CO 5σ orbital and Ni $3d_{z^2}$ band in the bottom of the valence band (donation). In addition, there is weak hybridization between CO $2\pi^*$ and Ni $3d_{x^2-y^2}$ in the conduction band (back donation). The fact that both hybridizations appear far from the Fermi level rationalizes well the weak binding strength of adsorbed CO.

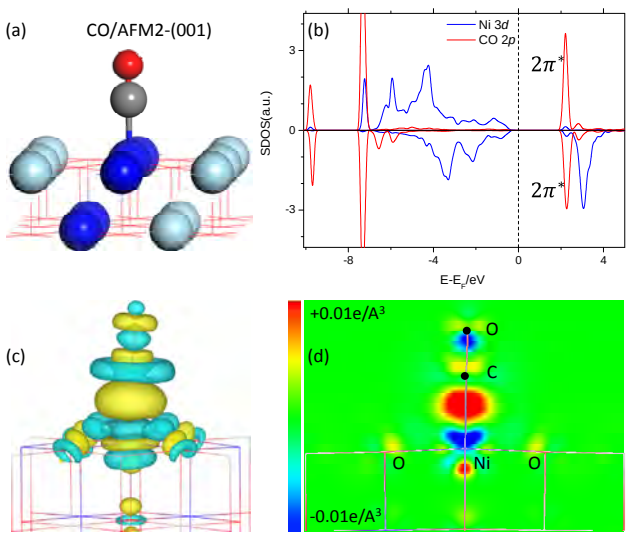

Fig. 5. CO adsorption on NiO AFM2(001). (a) Adsorption configuration; (b) SDOS of Ni 3*d* and CO 2*p* orbitals; (c) Isosurface view; (d) Section contour view of difference of electron density for CO adsorption. For isosurface view, yellow/green color means electron accumulation/depletion respectively.

Direct visualization of the bonding between CO and Ni can be better seen from the difference of electron density (Figure 5(c) and (d)). Pronounced charge accumulation between CO and coordinated Ni is observed, which indicates the dominating role of the donation interaction in CO adsorption on a NiO(001) surface.

Compared with the case for CO adsorption, NO binds more strongly to Ni with a tilted configuration (Figure 6(a)), in agreement with previous studies of NO adsorption on NiO(100) [38] and transition metal surfaces [49,50]. For instance, on AFM2-(001), the tilt angle is 10.7° for the Ni–N bond and 49.5° for the N–O bond. Depending on the magnetic phase (Table 4), the optimized Ni–N bond length varies in the range of 1.98–2.05 Å, and the configuration with a shorter Ni–N bond length is consistent with stronger binding. The N–O bond length (1.17–1.18 Å) is nearly the same as that of the gas phase (1.17 Å). After NO adsorption, the magnetic moments of NO and coordinated Ni decrease by about 0.10 and 0.20 μ_B, respectively. Interestingly, the magnetic moment of adsorbed NO is always antiparallel with coordinated Ni irrespective of the surfaces magnetic phase; this will be discussed further later.

Upon NO adsorption, the hybridization between the NO 5σ orbital and Ni $3d_{z^2}$ band in the bottom of the valence band decreases slightly (Figure 6(b)). Compared to the CO 2π* orbital, which is completely unoccupied, the NO 2π* orbital in the top of the valence band is partially occupied. For Ni(↑), it is mainly the Ni $3d_{xz,yz}$ spin-down component populated in the top/upper part of the valence band. To maximize the hybridization between NO 2π* and Ni $3d_{xz,yz}$ in the top/upper part of the valence band, the occupied NO 2π* must populate the spin-down component. In other words, the favorable configuration of magnetic moment between NO and coordinated Ni is antiparallel, namely, NO(↓) and coordinated Ni(↑), which is also found for NO adsorption on NiO(011).

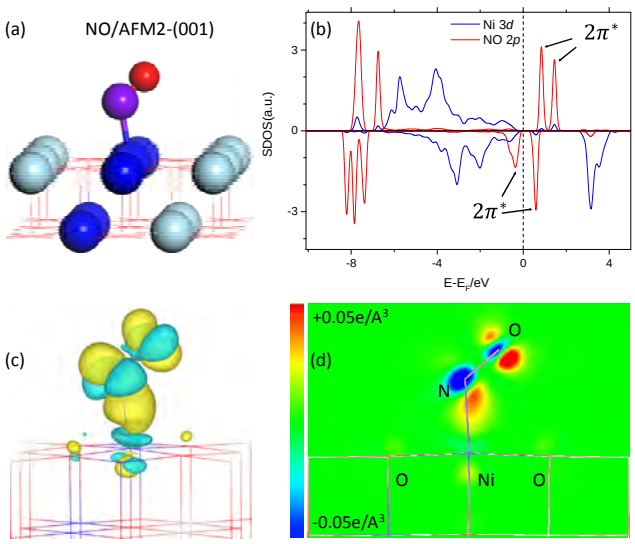

Fig. 6. NO adsorption on AFM2(001). (a) Adsorption configuration; (b) SDOS of Ni 3*d* and NO 2*p* orbitals; (c) Isosurface view; (d) Section contour view of difference of electron density for NO adsorption. For isosurface view, yellow/green color means electron accumulation/depletion respectively.

Table 4
Magnetism and structure information of NO adsorption on NiO {001} surfaces. Magnetic moment (M_{Ni}, M_{NO}) is given in unit of μ_B. Adsorption energy of NO (E_{ads}) is given in eV. Bond length ($d_{Ni\text{-}N}$) is given in Å.

	$M_{Ni(clean)}(\uparrow)/\mu_B$	$M_{Ni}(\uparrow)/\mu_B$	$M_{NO}(\downarrow)/\mu_B$	$d_{Ni\text{-}N}$/Å	E_{ads}/eV
AFM1(001)	1.80	1.63	−0.61	2.00	−0.45
AFM1(100)	1.81	1.63	−0.61	2.00	−0.46
AFM2(001)	1.72	1.56	−0.58	2.05	−0.42
AFM3(001)	1.78	1.62	−0.63	2.01	−0.44
AFM3(100)	1.77	1.59	−0.60	1.98	−0.45
AFM4(001)	1.78	1.62	−0.62	2.00	−0.44
AFM4(100)	1.77	1.59	−0.57	1.98	−0.45
AFM5(001)	1.74	1.56	−0.61	1.98	−0.45
AFM5(100)	1.75	1.58	−0.58	1.99	−0.44
FM(001)	1.80	1.63	−0.56	1.99	−0.45

Regarding the decrease of the magnetic moment of adsorbed NO, we note that the peak intensity of NO 2π* at the top of the valence band is smaller than those of the three other peaks of NO 2π* in the conduction band. This indicates the electron depletion in the corresponding states (spin-down component), and accordingly, the NO magnetic moment decreases. Similarly, the decrease of the magnetic moment of coordinated Ni can be rationalized by the depletion of Ni $3d_{z^2}$ states (lower peak intensity) at the bottom of the valence band (spin-up component).

Compared to CO adsorption, the extra hybridization between NO 2π* and Ni $3d_{xz,yz}$ in the valence band strengthens the binding between NO and the coordinated Ni atom. The direct participation of the NO 2π* orbital can be clearly seen from the difference of electron density plotted in Figure 6(c) and (d). Moreover, the magnitude of the difference of electron density induced by NO adsorption is about five times larger than that of CO (Figure 6(d) versus Figure 5(d)). The larger extent of electron redistribution induced by NO than by CO corroborates well with its stronger binding strength. For both CO adsorption (Figure 6(c) and (d)) and NO adsorption (Figure 5(c) and (d)), the adsorption-induced charge redistribution is limited to the singly coordinated Ni atom, and electrons of the NN Ni are hardly affected. In other words, the long-range magnetic phase has little influence on NO and CO adsorption on NiO(001).

3.3. NiO(011)

3.3.1. Surface properties

Without considering the magnetic phases, the {011} plane family consists of twelve equivalent planes. When taking into account the magnetism, the symmetry and degeneracy are broken. As listed in Table 5 and plotted schematically in Figure 7, for AFM1, AMF2, AFM3, and AFM4, there are two nonequivalent surfaces, and for AFM5, there are three inequivalent surfaces. This gives a total of eleven nonequivalent surfaces. For nonequivalent AFM1-(011), AFM2-(01$\bar{1}$), AFM3-(110), and AFM5-(10$\bar{1}$) surfaces, the local magnetic moments of the two adjacent surface Ni atoms are exclusively antiparallel (↑↓). Conversely, for nonequivalent AFM1-(110), AFM2-(011), AFM4-(110), and AFM5-(101) surfaces, the local magnetic

Table 5
Nonequivalent surface of rock salt NiO{011} plane family taking into account of magnetism. The surface in each column remains equivalent from each other. Corresponding surface energy γ (meV/Å^2) is given, and as reference for FM NiO(011), γ = 165 meV/Å^2.

	AFM1		AFM2		AFM3		AFM4		AFM5		
γ	162	163	172	172	166	165	167	167	169	170	170
	(011)	(110)	(011)	(01$\bar{1}$)	(011)	(110)	(011)	(110)	(011)	(101)	(10$\bar{1}$)
	(0$\bar{1}$1)	($\bar{1}$10)	(0$\bar{1}$1)	(0$\bar{1}$1)	(0$\bar{1}$1)	($\bar{1}$10)	(0$\bar{1}$1)	($\bar{1}$10)	(0$\bar{1}$1)	($\bar{1}$0$\bar{1}$)	($\bar{1}$01)
	(0$\bar{1}$1)	($\bar{1}$10)	(101)	(10$\bar{1}$)	(01$\bar{1}$)	($\bar{1}$10)	(01$\bar{1}$)	($\bar{1}$10)	(01$\bar{1}$)		
	(01$\bar{1}$)	(1$\bar{1}$0)	($\bar{1}$0$\bar{1}$)	($\bar{1}$01)	(0$\bar{1}$1)	($\bar{1}$10)	(0$\bar{1}$1)	($\bar{1}$10)	(0$\bar{1}$1)		
	(101)		(110)	(1$\bar{1}$0)	(101)		(101)		(110)		
	($\bar{1}$0$\bar{1}$)		($\bar{1}\bar{1}$0)	($\bar{1}$10)	($\bar{1}$0$\bar{1}$)		($\bar{1}$0$\bar{1}$)		($\bar{1}\bar{1}$0)		
	(10$\bar{1}$)				(10$\bar{1}$)		(10$\bar{1}$)		(1$\bar{1}$0)		
	($\bar{1}$01)				($\bar{1}$01)		($\bar{1}$01)		($\bar{1}$10)		

moments of two adjacent surface Ni atoms are exclusively parallel (↑↑). For the nonequivalent AFM3-(011), AFM4-(011), and AFM5-(011) surfaces, both (↑↓) and (↑↑) pairs (noted as X1 and X2, respectively) coexist.

The calculated energies of {011} surfaces are summarized in Table 5. For the nonequivalent surfaces, the calculated surface energies vary from 162 to 172 meV/Å^2. These energies are about three times larger than those of NiO{001}, because more Ni–O bonds (per unit area) are broken to create the new surface from the bulk material. In contrast, the surface energies of the nonequivalent surfaces belonging to the same AFM phase differ only by 1 meV/Å^2. This means that the variation of the surface energies by 10 meV/Å^2 mainly originates from the different long-range magnetic phases. Although the absolute variation of surface energies is about twice that of NiO{001} surfaces, the contribution to the overall surface energies remains small (~6%). This shows again the weak effect of the magnetic phases on surface energies.

Figure 8 plots the SDOS of a surface Ni atom (↑) of AFM2-(011). The $3d_{x^2-y^2}$ and $3d_{yz}$ states are populated mainly in the bottom of the valence band (spin up) and the lower part of

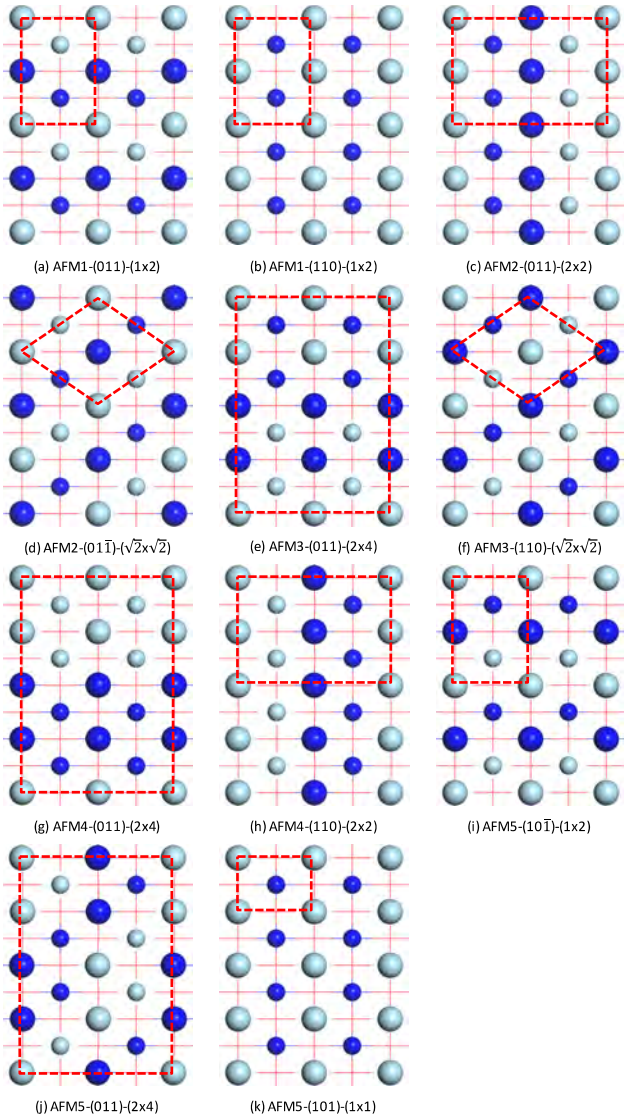

Fig. 7. Top view configuration of nonequivalent NiO(110) surfaces taking into account of magnetism. Ni atoms at top and second layer are presented with larger and smaller ball, respectively.

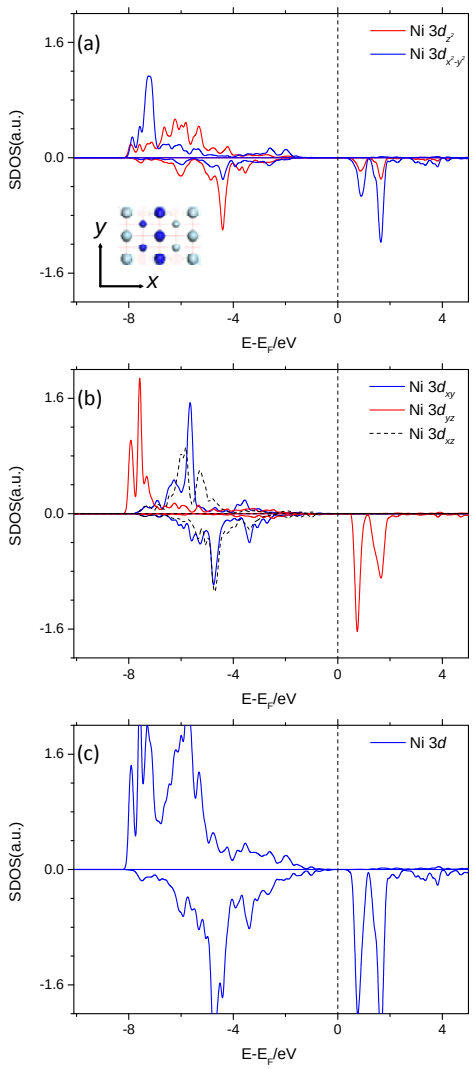

Fig. 8. Spin-resolved projected density of states (SDOS) for Ni of clean AFM2 NiO(011). (a) Total SDOS of Ni 3*d*; (b) SDOS projected onto Ni $3d_{z^2}$, $3d_{x^2-y^2}$; (c) SDOS projected onto Ni $3d_{xy}$, $3d_{yz}$, $3d_{xz}$. The reference coordinates for SDOS projection is shown in inset of (a), where *x*-axis represents for [100] direction and *y*-axis for [01$\bar{1}$] direction.

the conduction band (spin down), while $3d_{z^2}$, $3d_{xz}$, and $3d_{xy}$ are populated in the valence band. The upper part of the valence band originates largely from Ni $3d_{xy,xz}$ (spin down). Another prominent feature is the gap between the VBM and CBM of the Ni 3*d* band of 1.40 eV, which is much smaller than that of AFM2-(001) (2.81 eV) and AFM2 bulk (3.23 eV). The smaller 3*d* band gap of the surface Ni might facilitate its hybridization with adsorbed molecules, which will be discussed below.

3.3.2. CO adsorption

CO adsorption on these nonequivalent surfaces was studied, and the results at the most favorable sites are listed in Table 6. CO prefers to adsorb exclusively via the end of the C atom at the bridge site of two adjacent Ni atoms, labeled as A and B (Figure 9(a) and (c)). Irrespective of the nonequivalent surfaces and different bridge sites (↑↑ and ↑↓) considered, CO has similar adsorption energies at the (↑↓) bridge sites (Figure 9(e)); the calculated adsorption energies vary from −0.73 to −0.75 eV. Conversely, for CO adsorption at the (↑↑) bridge sites (Figure 9(b)), the calculated adsorption energies are smaller (−0.71 to −0.72 eV). Thus, the local magnetic moment and its relative direction of two coordinated Ni atoms are responsible for the variation of the calculated adsorption energies rather than the long-range magnetic phases. The calculated binding strengths of CO on NiO {011} are about twice that of CO on NiO{001}, which possibly arises from the greater number of Ni–C bonds involved and the lower coordination number of surface Ni atoms.

Important geometrical parameters and the bond lengths between C and two coordinated Ni atoms are given in Table 6. The optimized C–Ni bond lengths are in the range of 2.13–2.23 Å, and longer than those of CO adsorbed on NiO(001) (2.02–2.07 Å). Irrespective of the magnetic phases considered, the C–O bond lengths stayed at a constant value of 1.15 Å, which is 0.01 Å longer than that of gas-phase CO. CO adsorption has little influence on the surface magnetism: the magnetic moment for CO and coordinated Ni atoms decreased by only about 0.02 and 0.05 μ_B, respectively.

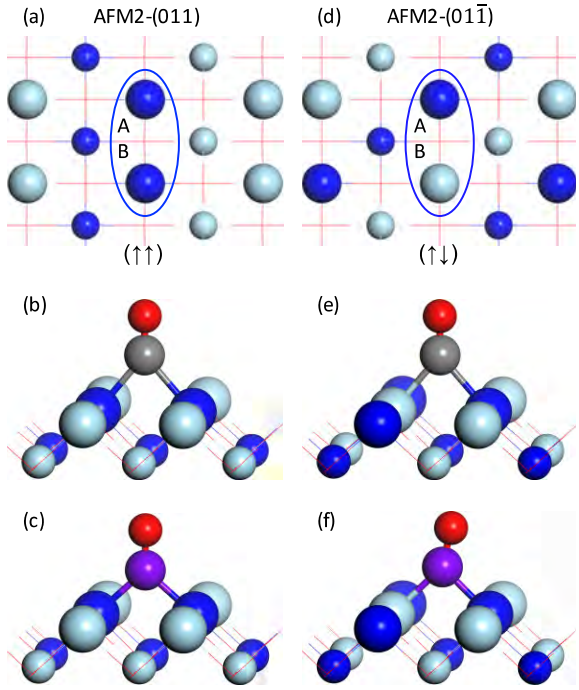

Fig. 9. Adsorption of CO/NO on NiO AFM2(011) and AFM2(01$\bar{1}$). (a) AFM2(011) surface with bridge sites of Ni(A, ↑) and Ni(B, ↑); (b) CO and (c) NO adsorbed configuration on AFM2(011); (d) AFM2(01$\bar{1}$) surface with bridge sites of Ni(A, ↑) and Ni(B, ↓); (e) CO and (f) NO adsorbed configuration on AFM2(01$\bar{1}$).

SDOS for CO adsorption at the (↑↑)-bridge sites of AFM2 NiO(011) are plotted in Figure 10(a). The magnetic moments of

Table 6
Magnetism and structure information of CO adsorption at the (↑↑)-bridge and (↑↓)-bridge sites of NiO {011} surfaces. Ni(A) always labels the Ni with total magnetic moment spin up. Magnetic moment (M_{Ni}, M_{CO}) is given in unit of μ_B. Bond length ($d_{Ni\text{-}C}$) is given in Å. Adsorption energy of CO (E_{ads}) is given in eV.

	$M_{Ni(clean)}/\mu_B$	$M_{Ni(A)}/\mu_B$	$M_{Ni(B)}/\mu_B$	M_{CO}/μ_B	$d_{Ni(A)\text{-}C}$/Å	$d_{Ni(B)\text{-}C}$/Å	E_{ads}/eV
(↑↓)-bridge		(↑)	(↓)				
AFM1(011)	1.77	1.72	−1.72	0.01	2.13	2.15	−0.73
AFM2(01$\bar{1}$)	1.70	1.66	−1.66	0.00	2.18	2.18	−0.74
AFM3(011)X1	1.75	1.73	−1.73	0.04	2.19	2.16	−0.75
AFM3(110)	1.74	1.68	−1.68	0.00	2.13	2.13	−0.74
AFM4(011)X1	1.75	1.72	−1.72	−0.05	2.16	2.19	−0.72
AFM5(011)X1	1.72	1.67	−1.66	0.00	2.14	2.12	−0.74
AFM5(10$\bar{1}$)	1.72	1.67	−1.66	−0.01	2.14	2.12	−0.74
(↑↑)-bridge		(↑)	(↑)				
AFM1(110)	1.78	1.74	1.74	0.02	2.17	2.17	−0.71
AFM2(011)	1.70	1.68	1.68	0.03	2.17	2.19	−0.71
AFM3(011)X2	1.75	1.72	1.72	0.05	2.18	2.19	−0.71
AFM4(011)X2	1.75	1.71	1.73	0.05	2.15	2.23	−0.71
AFM4(110)	1.74	1.69	1.69	0.00	2.15	2.14	−0.72
AFM5(011)X2	1.72	1.69	1.69	0.03	2.16	2.19	−0.71
AFM5(101)	1.73	1.70	1.70	0.06	2.18	2.17	−0.71
FM(011)	1.78	1.75	1.75	0.06	2.17	2.18	−0.71

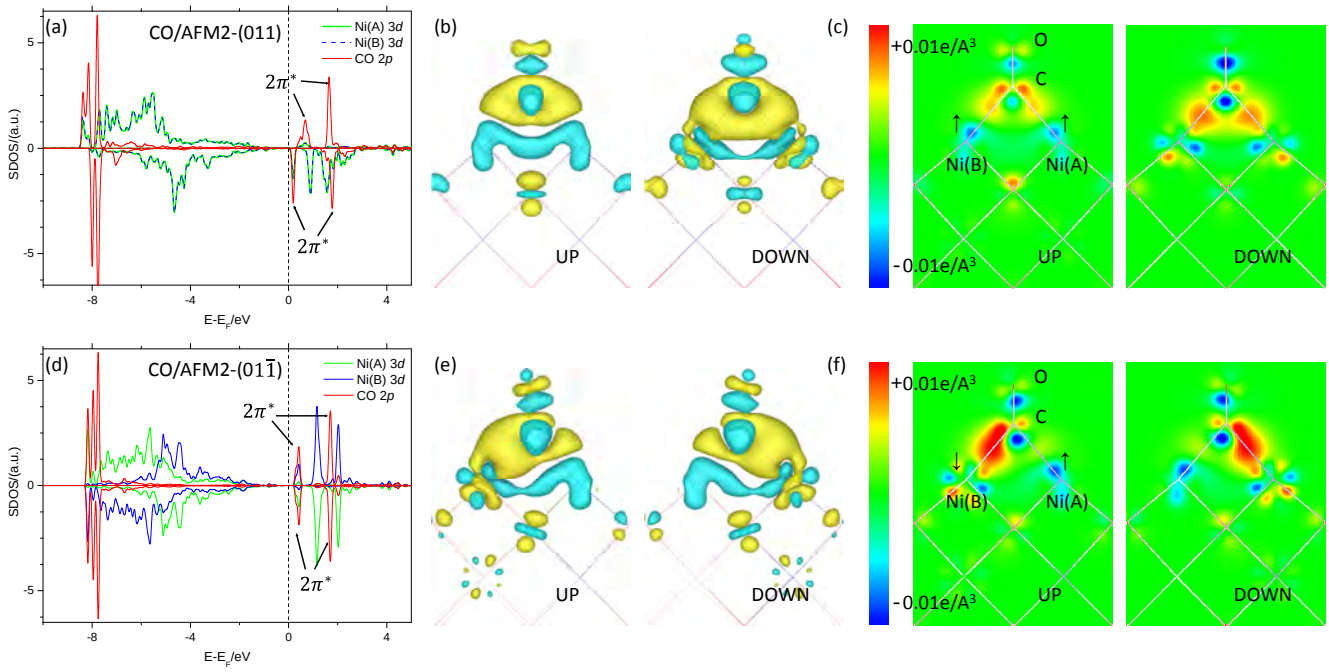

Fig. 10. CO adsorption on AFM2(011) and AFM2(01$\bar{1}$). (a–c) CO adsorption on AFM2(011); (d–f) CO adsorption on AFM2(01$\bar{1}$); (a, d) SDOS for 3*d* orbitals of Ni(A) and Ni(B) labeled in Figure 9 and 2*p* orbitals of CO; (b, e) Isosurface view and (c, f) section contour view of spin-resolved difference of electron density for CO adsorption with spin-up component labeled UP and spin-down component labeled DOWN, respectively.

both Ni(A) and Ni(B) point upwards, which are denoted as Ni(A, ↑) and Ni(B, ↑), respectively. Figure 10(a) reveals that the spin-up components of Ni(A, ↑) and Ni(B, ↑) are nearly completely occupied. The hybridization occurs mainly via Ni(A, ↑)/Ni(B, ↑) back-donation towards CO. In contrast, the spin-down components of Ni(A, ↑) and Ni(B, ↑) are partially occupied, and hybridization occurs via CO donation to Ni(A, ↑)/Ni(B, ↑). Back donation in the spin-up component but donation in the spin down can be easily visualized in the spin-resolved difference of electron density results plotted in Figure 10(b) and (c). For the spin-up case, there is pronounced charge depletion from both Ni(A, ↑) and Ni(B, ↑) and accumulation in CO $2\pi^*$ (back donation). For the spin-down component, there is charge depletion caused by CO 5σ donation and accumulation mainly between CO and Ni(A, ↑)/Ni(B, ↑).

SDOS for CO adsorption at the (↑↓) bridge sites of AFM2(01$\bar{1}$) are plotted in Figure 10(d), where the magnetic moments of Ni(A) and Ni(B) respectively point upwards (↑) and downwards (↓), and are denoted as Ni(A, ↑) and Ni(B, ↓), respectively. For the spin-up component, Ni(A, ↑) is nearly fully occupied and Ni(B, ↓) is partially occupied. Accordingly, the hybridization takes place via Ni(A, ↑) back donation toward CO, but CO donation toward Ni(B, ↓). This can be observed in the spin-resolved difference of electron density of the system (Figure 10(e) and (f)). There is modest charge depletion at Ni(A, ↑) for back donation and pronounced charge accumulation between CO and Ni(B, ↓) for CO donation. The relative larger extent of charge accumulation between CO and Ni(B, ↓) than that of charge depletion at Ni(A, ↑) indicates that donation rather than back donation plays a dominant role in the overall hybridization between CO and Ni. For the spin-down component (Figure 10(d)), Ni(B, ↓) is nearly fully occupied and Ni(A, ↓) is partially occupied. Accordingly, the hybridization takes place via Ni(B, ↓) back donation toward CO and CO donation toward Ni(A, ↑). The distinct hybridization and charge redistribution for CO at the (↑↓) bridge sites from that of the (↑↑) bridge sites is in contrast to their similar adsorption energies (which differ by less than 0.03 eV).

3.3.3. *NO adsorption*

NO adsorption also occurs preferentially at the bridge site of two adjacent Ni atoms via the end of the N atom (Figure 9(c) and (f)). For all nonequivalent surfaces considered, the calculated adsorption energies for NO at the (↑↓) bridge sites are in the range of −0.99 to −1.05 eV and in the range of −1.21 to −1.30 eV at the (↑↑) bridge sites. Different from CO, the binding strengths at the (↑↑) bridge sites are about 0.3 eV stronger than those at the (↑↓) bridge sites. Moreover, the NO binding strength on NiO(011) is about three times stronger than that of NiO(001). For adsorption on (↑↑) or (↑↓) bridge sites, the difference of adsorption energy with variation of bulk magnetic order and surface index is less than 0.10 eV. In contrast, the variation of NO adsorption energy on all studied NiO(001) surfaces did not exceed 0.04 eV. This indicates that the larger variation of binding strength at all (↑↑) bridge sites (or (↑↓) bridge sites) of NiO(011) than that of NiO(001) may be simply caused by the higher surface activity of NiO(011). However, the difference of binding strength between adsorption at (↑↑) bridge sites and that at (↑↓) bridge sites of NiO(011) cannot be attributed to this reason. Again, the importance of the local magnetic order rather than the long-range magnetic phase is found here.

Important geometrical parameters for NO adsorption on NiO(011) are given in Table 7. Irrespective of the different magnetic phases considered, the N–O bond lengths stay constant at 1.19 Å, 0.02 Å longer than that of gas-phase NO. For NO adsorption at the (↑↑) bridge sites, the two N–Ni bond lengths are nearly same (1.96–1.97 Å). The corresponding NO magnetic moment prefers to align antiparallel with the two coordinated Ni(↑), namely, as NO(↓), as also found for NO adsorption on NiO(001). The magnetic moments of NO and coordinated Ni atoms decreased by at most 0.25 and 0.13 μ_B, respectively. For NO adsorption at the (↑↓) bridge sites, the two N–Ni bond lengths were not the same. The shorter one varied from 1.93 to 1.97 Å. The magnetic moments of NO and Ni corresponding to the shorter N–Ni bond pointed downwards (↓) and upwards (↑), decreasing by at most 0.43 and 0.20 μ_B, respectively. The longer N–Ni bond length varied from 2.03 to 2.09 Å, and there was little change of the magnetic moment of coordinated Ni(↓), which is understandable because of its relative longer N–Ni bond length.

Calculated SDOS for NO at the (↑↑) bridge sites of AFM2 NiO(011) is plotted in Figure 11(a), where the magnetic moments of both Ni(A) and Ni(B) point upwards and are denoted as Ni(A, ↑) and Ni(B, ↑), respectively. As noted above, the NO magnetic moment prefers to point downward (↓); namely, there are more electrons occupied in the NO spin-down component than in the spin-up component. More electrons in the NO spin-down component would facilitate the corresponding donation process. This was verified in the spin-resolved difference of electron density results plotted in Figure 11(b) and (c), where charge accumulated between NO and coordinated Ni(A, ↑)/Ni(B, ↑). For the spin-up component, less electron occupation of the NO orbital would facilitate the corresponding back donation. This can be found in Figure 11(b) and (c), where charge depleted from coordinated Ni(A, ↑)/Ni(B, ↑) and accumulated in the NO molecule.

Calculated SDOS for NO adsorbed at the (↑↓) bridge sites of AFM2(01$\bar{1}$) is plotted in Figure 11(d), where the magnetic moments of Ni(A) and Ni(B) point upwards and downwards and are denoted as Ni(A, ↑) and Ni(B, ↓), respectively. The N–O bond length with Ni(A, ↑) is shorter than that with Ni(B, ↓), and the NO magnetic moment points downward accordingly. The hybridization between NO(↓) and Ni(A, ↑) with antiparallel magnetic configuration is essentially the same as that for NO adsorption on AFM2(011) because the electronic and magnetic configurations are the same. This can be seen further in the corresponding difference of electron density plots (Figure 11 (e) and (f)). Conversely, for NO(↓) and Ni(B, ↓) with same orientation of magnetic moments, the electronic hybridization between NO and Ni(B) is limited. Indeed, the difference of electron density (Figure 11(e) and (f)) between NO and Ni(B) becomes negligible, particularly in the spin-down component. This rationalizes well the weaker binding strength of NO adsorption at the (↑↓) bridge sites than that of NO at the (↑↑) bridge sites.

4. Conclusions

By constructing surface models of NiO with different magnetic phases, and using the paramagnetic molecule NO and nonparamagnetic molecule CO to probe the reactivity on (001) and (011) surfaces, we investigated the influence of magnetism on the surface chemistry of NiO. When the favorable adsorption sites involve only a single Ni cation, such as NO/CO adsorption at the top site of a Ni cation on the (001) surface, the long-range magnetic phases make little contribution to the overall adsorption behavior. The adsorption strength is primarily determined by chemical environment (such as surface orientation, coordination number, and adsorbed species). When the favorable

Table 7
Magnetism and structure information of NO adsorption at the (↑↑)-bridge and (↑↓) bridge sites of NiO {011} surfaces. Ni(A) always labels the Ni with total magnetic moment spin up. Magnetic moment (M_{Ni}, M_{NO}) is given in unit of μ_B. Bond length ($d_{Ni\text{-}N}$) is given in Å. Adsorption energy of NO (E_{ads}) is given in eV.

	$M_{Ni(clean)}/\mu_B$	$M_{Ni(A)}/\mu_B$	$M_{Ni(B)}/\mu_B$	M_{NO}/μ_B	$d_{Ni(A)\text{-}N}$/Å	$d_{Ni(B)\text{-}N}$/Å	E_{ads}/eV
(↑↓)-bridge		(↑)	(↓)	(↓)			
AFM1(011)	1.77	1.58	−1.74	−0.47	1.93	2.03	−1.05
AFM2(01$\bar{1}$)	1.70	1.56	−1.71	−0.39	1.96	2.07	−1.01
AFM3(011)X1	1.75	1.54	−1.79	−0.64	1.95	2.08	−1.01
AFM3(110)	1.74	1.53	−1.78	−0.74	1.96	2.09	−1.05
AFM4(011)X1	1.75	1.57	−1.78	−0.65	1.97	2.05	−1.03
AFM5(011)X1	1.72	1.53	−1.75	−0.63	1.96	2.07	−1.02
AFM5(10$\bar{1}$)	1.72	1.54	−1.73	−0.30	1.94	2.05	−0.99
(↑↑)-bridge		(↑)	(↑)	(↓)			
AFM1(110)	1.78	1.65	1.65	−0.68	1.97	1.97	−1.30
AFM2(011)	1.70	1.57	1.57	−0.61	1.97	1.97	−1.21
AFM3(011)X2	1.75	1.61	1.63	−0.49	1.96	1.97	−1.26
AFM4(011)X2	1.75	1.61	1.74	−0.47	1.96	1.97	−1.26
AFM4(110)	1.74	1.61	1.61	−0.72	1.96	1.96	−1.30
AFM5(011)X2	1.72	1.58	1.59	−0.53	1.96	1.97	−1.24
AFM5(101)	1.73	1.61	1.61	−0.53	1.97	1.97	−1.23
FM(011)	1.78	1.64	1.64	−0.59	1.96	1.96	−1.29

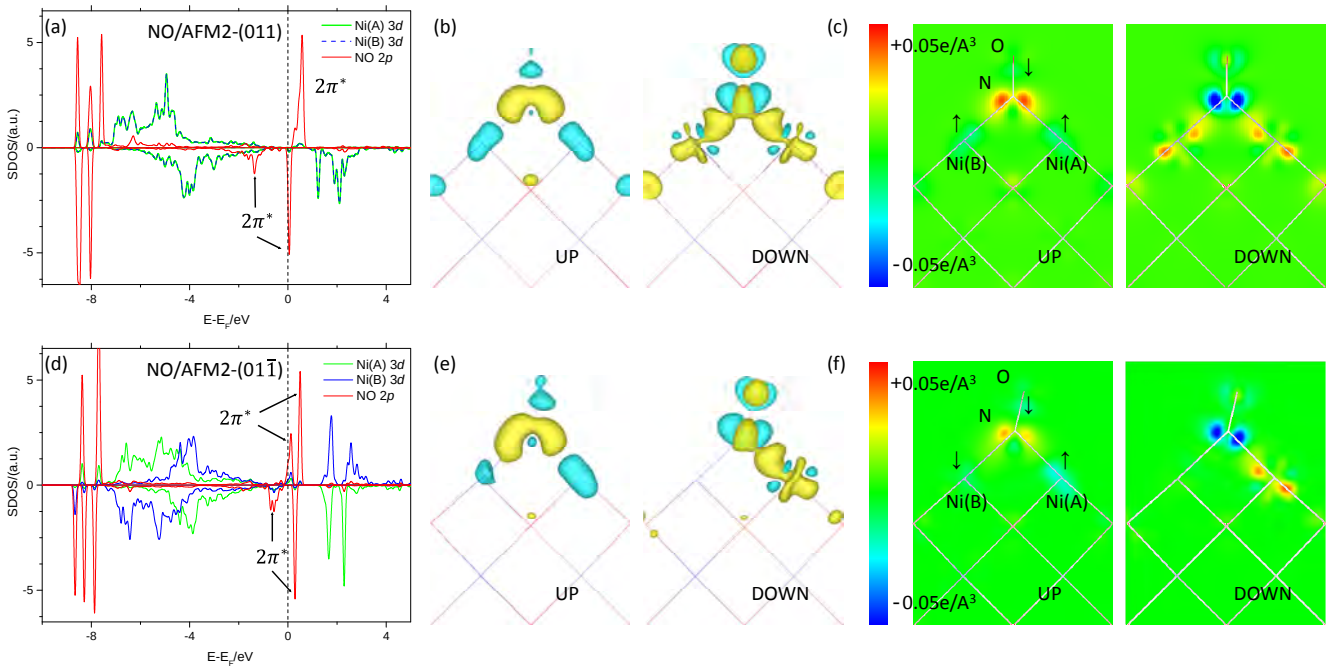

Fig. 11. NO adsorption on NiO AFM2(011) and AFM2(01$\bar{1}$). (a–c) NO adsorption on AFM2(011); (d–f) NO adsorption on AFM2(01$\bar{1}$); (a, d) SDOS for 3*d* orbitals of Ni(A) and Ni(B) labeled in Figure 9 and 2*p* orbitals of NO; (b, e) Isosurface view and (c, f) section contour view of spin-resolved charge flow diagram for NO adsorption with spin-up component labeled UP and spin-down component labeled DOWN, respectively.

adsorption site involves two adjacent Ni cations, such as NO/CO adsorption at the bridge site of two Ni cations in NiO(011), the local magnetic order of Ni ions coordinated to the adsorbed molecule rather than the long-range magnetism makes a considerable contribution to the overall adsorption behavior. For nonparamagnetic molecule CO, the orbital hybridization for adsorption at the (↑↑) bridge sites is very different from that at the (↑↓) bridge sites, despite their incidental similar adsorption energies. For paramagnetic molecule NO, the hybridization at the (↑↑) bridge sites is different from that at the (↑↓) bridge sites, and the binding strength of the former is about 0.3 eV stronger than that of the latter. The present work highlights the importance of the local magnetic order of TMO surfaces on molecule adsorption, particularly for paramagnetic molecules, at multi-fold sites.

Acknowledgments

We are grateful for the fruitful discussion with Prof. Hong Jiang.

References

[1] U. Diebold, S. C. Li, M. Schmid, *Annu. Rev. Phys. Chem.*, **2010**, 61, 129–148.
[2] J. F. Weaver, *Chem. Rev.*, **2013**, 113, 4164–4215.
[3] G. A. Somorjai, Y. M. Li, *Proc. Natl. Acad. Sci. USA*, **2011**, 108, 917–924.
[4] S. Shaikhutdinov, H. J. Freund, *Annu. Rev. Phys. Chem.*, **2012**, 63, 619–633.

Graphical Abstract

Chin. J. Catal., 2017, 38: 1736–1748 doi: 10.1016/S1872-2067(17)62883-3

Influence of nickel(II) oxide surface magnetism on molecule adsorption: A first-principles study

Chuan-Qi Huang, Wei-Xue Li *
Dalian Institute of Chemical Physics, Chinese Academic of Sciences;
University of Chinese Academy of Sciences;
University of Science and Technology of China

Calculations revealed that NO preferentially binds to Ni surfaces with its magnetic moment antiparallel to that of Ni. NO adsorbed at antiferromagnetic bridge sites binds to one Ni optimally and another in a frustrated manner.

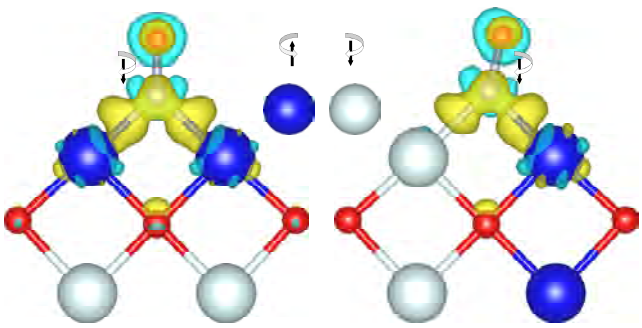

[5] H. Kuhlenbeck, S. Shaikhutdinov, H. J. Freund, *Chem. Rev.*, **2013**, 113, 3986–4034.
[6] D. P. Woodruff, *Chem. Rev.*, **2013**, 113, 3863–3886.
[7] S. M. Zhou, X. B. Miao, X. Zhao, C. Ma, Y. H. Qiu, Z. P. Hu, J. Y. Zhao, L. Shi, J. Zeng, *Nat. Commun.*, **2016**, 7, 11510.
[8] J. Suntivich, K. J. May, H. A. Gasteiger, J.B. Goodenough, Y. Shao-Horn, *Science*, **2011**, 334, 1383–1385.
[9] S. Chretien, H. Metiu, *J. Chem. Phys.*, **2008**, 129, 074705/1–074705/16.
[10] J. Behler, B. Delley, S. Lorenz, K. Reuter, M. Scheffler, *Phys. Rev. Lett.*, **2005**, 94, 036104/1–036104/4.
[11] E. Torun, C. M. Fang, G. A. de Wijs, R. A. de Groot, *J. Phys. Chem. C*, **2013**, 117, 6353–6357.
[12] R. V. Mom, J. Cheng, M. T. M. Koper, M. Sprik, *J. Phys. Chem. C*, **2014**, 118, 4095–4102.
[13] N. C. Tombs, H. P. Rooksby, *Nature*, **1950**, 165, 442–443.
[14] J. S. Smart, S. Greenwald, *Phys. Rev.*, **1951**, 82, 113–114.
[15] M. Finazzi, L. Duò, F. Ciccacci, *Surf. Sci. Rep.*, **2009**, 64, 139–167.
[16] M. Finazzi, L. Duò, F. Ciccacci, in: *Magnetic Properties of Antiferromagnetic Oxide Materials*, Wiley-VCH, **2010**, 1–23.
[17] P. W. Anderson, *Phys. Rev.*, **1950**, 79, 350–356.
[18] H. X. Deng, J. B. Li, S. S. Li, J. B. Xia, A. Walsh, S. H. Wei, *Appl. Phys. Lett.*, **2010**, 96, 162508/1–162508/3.
[19] A. Schrön, C. Rödl, F. Bechstedt, *Phys. Rev. B*, **2010**, 82, 165109/1–165109/12.
[20] T. Archer, C. D. Pemmaraju, S. Sanvito, C. Franchini, J. He, A. Filippetti, P. Delugas, D. Puggioni, V. Fiorentini, R. Tiwari, P. Majumdar, *Phys. Rev. B*, **2011**, 84, 115114/1–115114/14.
[21] C. G. Shull, W. A. Strauser, E. O. Wollan, *Phys. Rev.*, **1951**, 83, 333–345.
[22] U. Kaiser, A. Schwarz, R. Wiesendanger, *Nature*, **2007**, 446, 522–525.
[23] M. Granovskij, A. Schrön, F. Bechstedt, *Phys. Rev. B*, **2013**, 88, 184416/1–184416/5.
[24] F. Pielmeier, F. J. Giessibl, *Phys. Rev. Lett.*, **2013**, 110, 266101/1–266101/5.
[25] M. Granovskij, A. Schrön, F. Bechstedt, *New J. Phys.*, **2014**, 16, 23020/1–23020/18.
[26] A. Schrön, F. Bechstedt, *Phys. Rev. B*, **2015**, 92, 165112/1–165112/11.
[27] I. Sugiyama, N. Shibata, Z. C. Wang, S. Kobayashi, T. Yamamoto, Y. Ikuhara, *Nat. Nanotechnol.*, **2013**, 8, 266–270.
[28] H. Bi, S. D. Li, Y. C. Zhang, Y. W. Du, *J. Magn. Magn. Mater.*, **2004**, 277, 363–367.
[29] V. N. Antonov, L. V. Bekenov, A. N. Yaresko, *Adv. Cond. Matter Phys.*, **2011**, 2011, 1–107.
[30] P. Thunstrom, I. Di Marco, O. Eriksson, *Phys. Rev. Lett.*, **2012**, 109, 186401/1–186401/5.
[31] L. H. Ye, R. Asahi, L. M. Peng, A. J. Freeman, *J. Chem. Phys.*, **2012**, 137, 154110/1–154110/7.
[32] H. Jiang, R. I. Gomez-Abal, P. Rinke, M. Scheffler, *Phys. Rev. B*, **2010**, 82, 045108/1–045108/16.
[33] K. Terakura, T. Oguchi, A. R. Williams, J. Kübler, *Phys. Rev. B*, **1984**, 30, 4734–4747.
[34] V. I. Anisimov, J. Zaanen, O. K. Andersen, *Phys. Rev. B*, **1991**, 44, 943–954.
[35] S. L. Dudarev, G. A. Botton, S. Y. Savrasov, C. J. Humphreys, A. P. Sutton, *Phys. Rev. B*, **1998**, 57, 1505–1509.
[36] F. Manghi, V. Boni, *J. Electron. Spectrosc. Relat. Phenom.*, **2015**, 200, 181–192.
[37] A. Rohrbach, J. Hafner, G. Kresse, *Phys. Rev. B*, **2004**, 69, 075413/1–075413/13.
[38] A. Rohrbach, J. Hafner, *Phys. Rev. B*, **2005**, 71, 045405/1–045405/7.
[39] W. Zhao, M. Bajdich, S. Carey, A. Vojvodic, J. K. Nörskov, C. T. Campbell, *ACS Catal.*, **2016**, 6, 7377–7384.
[40] G. Kresse, J. Furthmuller, *Comp. Mater. Sci.*, **1996**, 6, 15–50.
[41] P. E. Blöchl, *Phys. Rev. B*, **1994**, 50, 17953–17979.
[42] G. Kresse, D. Joubert, *Phys. Rev. B*, **1999**, 59, 1758–1775.
[43] J. P. Perdew, K. Burke, M. Ernzerhof, *Phys. Rev. Lett.*, **1996**, 77, 3865–3868.
[44] S. H. Wei, A. Zunger, *Phys. Rev. B*, **1993**, 48, 6111–6115.
[45] T. Oguchi, K. Terakura, A. R. Williams, *Phys. Rev. B*, **1983**, 28, 6443–6452.
[46] M. Schönnenbeck, D. Cappus, J. Klinkmann, H. J. Freund, L. G. M. Petterson, P. S. Bagus, *Surf. Sci.*, **1996**, 347, 337–345.
[47] A. Zecchina, D. Scarano, S. Bordiga, G. Ricchiardi, G. Spoto, F. Geobaldo, *Catal. Today*, **1996**, 27, 403–435.
[48] R. Wichtendahl, M. Rodriguez-Rodrigo, U. Hartel, H. Kuhlenbeck, H. J. Freund, *Phys. Status Solidi A*, **1999**, 173, 93–100.
[49] Z. H. Zeng, J. L. F. Da Silva, H. Q. Deng, W. X. Li, *Phys. Rev. B*, **2009**, 79, 205413/1–205413/13.
[50] Z. H. Zeng, J. L. Da Silva, W. X. Li, *Phys. Chem. Chem. Phys.*, **2010**, 12, 2459–2470.

NiO表面磁性对分子吸附的影响的第一性原理研究

黄传奇[a,b], 李微雪[a,b,c,*]

[a]中国科学院大连化学物理研究所催化基础国家重点实验室, 辽宁大连116023

[b]中国科学院大学, 北京100049

[c]中国科学技术大学化学与材料科学学院化学物理系, 合肥微尺度物质科学国家重点实验室(筹), 安徽合肥230026

摘要: 过渡金属氧化物广泛应用在当今能源与环境相关的催化领域, 理解其表面化学性质以及结构-反应活性之间的关系对于先进催化材料的进一步发展以至理性设计至关重要. 3*d*后过渡系金属(Mn, Fe, Co, Ni)的氧化物以其中金属离子独特的自旋状态和由此产生的铁磁/反铁磁性为典型特征. 研究过渡金属氧化物的自旋状态以及磁性对表面化学的影响将使我们更加完整了解这些材料的表面化学. 以NiO为代表的后过渡系金属岩盐结构一元氧化物具有反铁磁性, 被经常作为反铁磁研究的模型体系. 尽管在低温(低于其Neel温度)下NiO体相的完整晶体具有确定的反铁磁序, 但是一系列最新研究表明, 在条件变化时NiO表面的Ni离子可以产生不同的磁序. 以此为背景, 本工作以NiO为模型体系, 采用DFT+U的第一性原理方法研究了NiO表面磁序对表面的小分子吸附活性的影响, 包括表面吸附活性对各磁性相的表面取向以及吸附物种磁性的依赖关系. 我们考察了NiO的5种反铁磁相和一种铁磁相, 两个晶面NiO(001)和NiO(011), 顺磁性分子NO和非顺磁性分子

CO. 我们发现表面能受磁性的影响较轻微, NiO(001)面上从49到54 meV/Å^2, NiO(011)面上从162到172 meV/Å^2. 在NiO(001)面上, CO与NO都倾向于在Ni离子的顶位吸附. 对于不同的体相磁序与表面取向, CO吸附能的变化范围为–0.33 ~ –0.37 eV, NO吸附能的变化范围为–0.42 ~ –0.46 eV. 在NiO(011)表面, 两种分子都倾向于吸附在由两个Ni离子构成的桥位. 我们发现相对于NiO不同磁性相的体相长程磁序, 吸附位点处构成桥位的两个Ni离子的局部磁矩相对取向对于分子的吸附具有更加显著的影响. 计算得到NO在局部磁矩相对取向反平行(↑↓)吸附位点处的吸附能为–0.99 ~ –1.05 eV, 在局部磁矩相对取向平行(↑↑)吸附位点处吸附会增强, 吸附能为–1.21 ~ –1.30 eV. 对于CO, 尽管计算的吸附能在(↑↓)吸附位点(–0.73 ~ –0.75 eV)与在(↑↑)吸附位点(–0.71 ~ –0.72 eV)非常接近, 两种吸附位点处的CO吸附时分子轨道杂化方式以及吸附后CO的局域电子态密度却具有明显不同的特征. 本工作突出揭示了分子在过渡金属氧化物表面的多重吸附位点上吸附时吸附位点的局域磁矩相对取向对吸附性能的影响.

关键词: 磁性; 表面取向; 分子吸附; 第一性原理; 电子结构

收稿日期: 2017-05-27. 接受日期: 2017-06-26. 出版日期: 2017-10-05.

*通讯联系人. 电话: (0551)63600650; 电子信箱: wxli70@ustc.edu.cn

基金来源: 国家自然科学基金(91645202); 国家重点研发计划(2017YFB602205); 国家重点基础研究发展计划(2013CB834603); 中国科学院前沿科学重点研究项目(QYZDJ-SSW-SLH054).

本文的英文电子版由Elsevier出版社在ScienceDirect上出版(http://www.sciencedirect.com/science/journal/18722067).